A progeria-associated BAF-1 mutation modulates gene expression and accelerates aging in *C. elegans*

Raquel Romero-Bueno[1] (ORCID ID 0000-0001-7454-2759), Adrián Fragoso-Luna[1], (ORCID ID 0000-0003-0325-7293), Cristina Ayuso[1] (ORCID ID 0000-0002-7179-4309), Alan Kavsek[2] (ORCID ID 0009-0006-0310-6654), Christian G. Riedel[2,3] (ORCID ID 0000-0002-3689-8022), Jordan D. Ward[4] (ORCID ID 0000-0001-9870-8936) and Peter Askjaer[1] (ORCID ID 0000-0003-3192-4428)

AFFILIATIONS

[1] Andalusian Centre for Developmental Biology, Consejo Superior de Investigaciones Científicas (CSIC), Universidad Pablo de Olavide, Junta de Andalucía, Carretera de Utrera, km 1, 41013 Sevilla, Spain

[2] Department of Biosciences and Nutrition, Karolinska Institutet, Huddinge 14157, Sweden

[3] Faculty of Life Sciences: Food, Nutrition, and Health, Department of Nutritional Physiology, University of Bayreuth, 95326 Kulmbach, Germany

[4] Department of Molecular, Cell, and Developmental Biology, University of California-Santa Cruz, Santa Cruz, CA 95064, USA

Corresponding author: pask@upo.es

KEYWORDS

Aging, *BANF1*, Chromatin organization, Gene expression, NGPS, Nuclear lamina, Progeria, Stress resistance

ABSTRACT

Alterations in the nuclear envelope are linked to a variety of rare diseases termed laminopathies. These include both tissue specific and systemic diseases. A single amino acid substitution in human barrier to autointegration factor (BAF) at position 12 (A12T) causes Néstor-Guillermo Progeria Syndrome (NGPS). This premature ageing condition affects a variety of tissues, leading to growth retardation and severe skeletal defects, including scoliosis. Taking advantage of the conservation between human and *C. elegans* BAF proteins, we have modified the *baf-1* locus in *C. elegans* to mimic the human NGPS mutation (*baf-1(G12T)*). In this work, we characterized the phenotypes caused by the G12T mutation at molecular, cellular, and organismal scale. We found that the mutation induced multiple phenotypes related to fertility, lifespan, and stress resistance. Importantly, nuclear morphology deteriorated faster during aging in *baf-1(G12T)*, relative to wild-type animals, coinciding with an important hallmark of cells from progeria patients. Nuclear envelope accumulation of lamin and emerin was reduced whereas localization of BAF-1(G12T) was similar to wild-type BAF-1. We determined the chromatin binding profiles for wild-type and mutant BAF-1 and performed transcriptome analyses through tissue-specific DamID. Although the global profiles for wild-type and G12T BAF-1 resembled one another, we also identified many discrete regions with altered BAF-1(G12T) association. Most genes deregulated by the *baf-1(G12T)* mutation were characterized by a change in BAF-1 association, suggesting a direct relation between BAF-1 binding and gene expression. We conclude that *C. elegans* is a relevant model to understand how a mutation in an essential protein expressed throughout development triggers the appearance of symptoms in early childhood.

INTRODUCTION

The chromosomes in eukaryotic cells are physically enclosed by the nuclear envelope (NE), which protects them from mechanical stress and serves as an anchoring point for chromatin and associated factors (Manzo et al. 2022). The NE is composed of outer and inner nuclear membranes, the nuclear lamina, and nuclear pore complexes to facilitate nucleocytoplasmic transport. The nuclear lamina is a rigid meshwork that consists mainly of intermediate filament proteins called lamins as well as a variety of lamin-associated proteins, including integral inner nuclear membrane proteins. Nuclear organization is dynamic and changes during development and aging. Moreover, chromatin is differently organized in the diverse cell types within an organism (Ungricht and Kutay 2017). Furthermore, both environmental stress factors (such as temperature, pathogens, or nutrient availability) and internal factors (like cellular stress and mutations) can provoke changes in nuclear organization and gene expression. It is therefore not surprising that NE alterations are related to dramatic human conditions and attract intensive biomedical research efforts (Dobrzynska et al. 2016b; Shin and Worman 2022; Fragoso-Luna and Askjaer 2023).

Barrier to Autointegration Factor 1 (BAF/BANF1) is a small (89 amino acids) chromatin binding protein enriched at the NE and highly conserved across metazoans (Sears and Roux 2020). BAF acts as a homodimer that binds simultaneously to DNA, lamins, and inner nuclear membrane LEM (LAP2, emerin, MAN1) domain proteins, thus serving as an anchoring factor (Bradley et al. 2005; Samson et al. 2018). BAF was initially discovered as a factor required for retroviral infectivity (Lee and Craigie 1998). Its depletion is lethal during embryogenesis in *Caenorhabditis elegans* and *Drosophila melanogaster* (Zheng et al. 2000; Furukawa et al. 2003; Margalit et al. 2005) and decreases the survival of mouse and human embryonic stem cells (Cox et al. 2011). The localization of BAF at the NE is interdependent of its interaction partners, including lamins (Margalit et al. 2005; Lin et al. 2020), and LEM domain proteins, although BAF is also present in the nucleoplasm and the cytoplasm (Haraguchi et al. 2001; Margalit et al. 2007). BAF localisation during the cell cycle is controlled by phosphorylation: at the entry to mitosis vaccinia-related kinase 1 (VRK1) phospholylates BAF, which reduces its affinity for chromatin (Nichols et al. 2006; Marcelot et al. 2021). The protein phosphatase 2 (PP2A) complex dephosphorylates BAF at the end of mitosis, allowing reassociation of BAF to chromatin and NE components (Asencio et al. 2012). Interfering with BAF phosphorylation has severe consequences: when VRK1 is depleted from *C. elegans* embryos or human cells, BAF remains associated with chromosomes when cells enter mitosis, which leads to defects in chromosome segregation (Gorjanacz et al. 2007; Molitor and Traktman 2014). BAF is required for mitotic chromosome coherence and nuclear assembly towards the end of mitosis (Gorjanacz et al. 2007; Samwer et al. 2017). It localizes on the surface of the condensed chromosomes to maintain these tightly together, thereby ensuring the reassembly of a NE that encompasses all chromosomes in a single nucleus (Haraguchi et al. 2008; Samwer et al. 2017). More recently, BAF was implicated in the repair of NE ruptures (Halfmann et al. 2019). BAF localizes to the rupture site by binding to the leaking chromatin, and recruits LEM domain proteins to repair the NE and restore the permeability barrier (Young et al. 2020; Kono et al. 2022; Barger et al. 2023). Finally, BAF has also been involved in sensing mechanical stimuli to regulate cell cycle progression and DNA replication (Wang et al. 2018; Unnikannan et al. 2020).

About a decade ago, an identical homozygous amino acid substitution in human BAF (A12T) was identified in 2 patients (Néstor and Guillermo) suffering from premature aging symptoms, leading to the term Néstor-Guillermo progeria syndrome (NGPS) (Puente et al. 2011). NGPS shares phenotypic similarities with Hutchinson-Gilford progeria syndrome (HGPS), which has been described in much greater detail and is most often caused by mutation in *LMNA* that encodes lamin A/C (Gonzalo et al. 2017). However, cardiovascular deficiencies and metabolic

complications have not been described for NGPS patients and the manifestation of the condition occurs later, approximately 24 months after birth (Cabanillas et al. 2011). Similarly to HGPS, nuclear morphology is abnormal in NGPS fibroblast, and can be restored by expression of wild-type BAF (Puente et al. 2011; Janssen et al. 2022). It was proposed that the mutation destabilizes BAF (Puente et al. 2011), although this has been questioned by others (Paquet et al. 2014). The residue mutated in NGPS is situated close to the interface with lamin and the mutation was reported to reduce the affinity between the two proteins (Samson et al. 2018; Janssen et al. 2022). However, another study found that ectopically expressed BAF A12T localized correctly to the NE, and that the mutation modulated the affinity of BAF for DNA, thus possibly interfering with chromatin anchoring at the NE (Paquet et al. 2014). The A12T mutation was demonstrated to also affects NE rupture repair. Although mutant BAF A12T accumulated at rupture sites allowing repair, nuclei were observed to suffer repeated rupture more frequently than in control cells (Janssen et al. 2022). Despite the identification of several cellular defects in NGPS cells, it remains unclear what eventually leads to the patient phenotypes after seemingly normal foetal and postnatal development.

Almost all studies described above were performed with cultured cells. Although the use of patient-derived cell lines is essential to answer many of the open questions about NGPS, cell lines suffer limitations in terms of interplay between tissues and different organs (Yamamoto et al. 2024). To study the effect of the NGPS mutation in a whole-animal model, we introduced the equivalent mutation in the endogenous *baf-1* locus in *C. elegans*. We show that *baf-1(G12T)* mutants recapitulate several phenotypes typical of progerias, including shortened lifespan and accelerated deterioration of nuclear morphology. Moreover, the mutants have reduced fertility, increased sensitivity to irradiation and temperature stress but, surprisingly, are more tolerant to oxidative stress. We observed numerous changes in BAF-1's association with chromatin in hypodermal and intestinal cells, suggesting that the G12T mutation affects the affinity of BAF-1 for chromatin. By focusing on *baf-1's* role in chromatin organization, we identified genes that are both deregulated and differentially bound by BAF-1(G12T). Enriched gene classes include structural components of cuticle and ribosomes, suggesting specific functions of BAF in the regulation of gene expression. We conclude that *baf-1(G12T)* mutants serve as a relevant model to advance our understanding of BAF function and the mechanisms underlying NGPS.

RESULTS

The *baf-1(G12T)* mutation reduces brood size and lifespan

C. elegans and human BAF proteins share 74% amino acid sequence similarity (Margalit et al. 2005) and are predicted to adopt identical three-dimensional structures (**Supplementary Figure S1A**), making the worm a suitable model to study BAF mutations. To evaluate the effect of the NGPS mutation on *C. elegans* health span parameters, we modified the endogenous *baf-1* locus to encode a threonine residue at position 12 instead of the naturally occurring glycine.

We first measured fertility. At 20°C, *baf-1(G12T)* self-fertilizing hermaphrodites produced the same number of descendants as control worms (**Figure 1A**). In contrast, when worms were shifted to 25°C before reaching adulthood, their fertility was reduced by 66% (**FIG 1B**, **Supplementary Figure S1B**), whereas embryonic viability was unaffected (**Supplementary Figure S1C**). We noticed that *baf-1(G12T)* hermaphrodites deposited many unfertilized oocytes (UFOs) on the plates at 25°C (**Figure 1B**). *C. elegans* hermaphrodites usually lay a few UFOs when they run out of sperm (produced during the larval L4 stage) at the end of their reproductive cycle (Collins et al. 2008). However, *baf-1(G12T)* mutants laid UFOs throughout the fertile period, representing a 34% of the total lay versus only 6% in control animals (**Figure 1B**). We investigated if the UFOs laid by *baf-1(G12T)* hermaphrodites at 25°C could be explained by a lack in sperm production. However, we found sperm with the same frequency in the spermatheca of control and *baf-1(G12T)* hermaphrodites on days 1 and 2 of adulthood (**Figure 1C, D**). On day 3, sperm

were still observed in approximately half of the control animals but in none of the *baf-1(G12T)* mutants. These data indicate that although sperm were produced there might be defects in function. To test this hypothesis, we mated *baf-1(G12T)* day 1 adult hermaphrodites with wild-type males at 25°C for 7 hours. After mating we did not observe UFOs and the brood size was comparable to self-fertilizing wild-type hermaphrodites (**Supplementary Figure S2A**). Mating *baf-1(G12T)* hermaphrodites with *baf-1(G12T)* males also eliminated UFOs, but did not fully restore the brood size, suggesting a sperm defect in *baf-1(G12T)* males (**Supplementary Figure S2A**). To test this possibility, we incubated *baf-1(G12T)* males with *fog-2(q71)* feminized worms at 25°C and counted daily offspring. Isogenic *fog-2(q71)* males were used as a control. We observed a reduction in brood size of approximately one third when sperm came from *baf-1(G12T)* males (**Supplementary Figure S2B, C**). The male/female ratio in the progeny was ~1, suggesting that meiotic segregation of chromosomes was normal in *baf-1(G12T)* males.

To gain insight into BAF-1 localization, we knocked GFP and mCherry (mCh) cassettes into the endogenous *baf-1* and *baf-1(G12T)* loci to generate N-terminal fusions. We observed that BAF-1 is present in mature sperm, both in males (**Supplementary Figure S3A**) and hermaphrodites (**Supplementary Figure S3B**). In nematode sperm, chromosomes are surrounded by a poorly defined halo that presumably lacks nuclear membranes (Wolf et al. 1978). GFP::BAF-1(G12T) is also visible in sperm in hermaphrodites (**Supplementary Figure S3C**), indicating that BAF-1's localization is not affected by the NPGS mimicking mutation. In contrast to BAF-1, we could not detect endogenously tagged LMN-1 or EMR-1 in sperm of hermaphrodites (**Supplementary Figure S3D**), nor LMN-1 in sperm in males (**Supplementary Figure S3E**). Moreover, the *baf-1(G12T)* mutation did not induce localization of GFP::LMN-1 to sperm (**Supplementary Figure S3F**).

We next evaluated if the NGPS mutation affected lifespan, as would be expected for a progeria model. At 20°C, *baf-1(G12T)* hermaphrodites lived as long as control animals (**Supplementary Figure S1D**). However, because lifespan correlates inversely with fertility (Arantes-Oliveira et al. 2002; Berman and Kenyon 2006), we speculated that the lower brood size in *baf-1(G12T)* at restrictive temperature might counteract a potential shortening of their lifespan. To address this, we first evaluated lifespan at 25°C in the presence and absence of the transcription factor DAF-16, which is required to correlate fecundity with longevity (Hsin and Kenyon 1999). As expected, depletion of DAF-16 reduced lifespan in wild-type hermaphrodites, as well as in *baf-1(G12T)* ($p < 2e^{-16}$; **Figure 1E**). Importantly, the *baf-1(G12T)* mutation caused a reduction in median lifespan at the restrictive temperature both in the presence (7% reduction; $p = 8e^{-13}$) and absence (9% reduction; $p = 7e^{-10}$) of DAF-16 (**Figure 1E**). To completely eliminate the confounding effect of the germ line on lifespan, we ablated the germ line by using the *glp-4(ts)* mutation, which prevents germ cell proliferation at 25°C (Beanan and Strome 1992). We found that median lifespan of sterile *glp-4(ts)* worms was reduced from 16 to 12 days (25% reduction; $p < 2e^{-16}$) by the *baf-1(G12T)* allele (**Figure 1F**). These data indicate that the NGPS mutation affects fecundity and lifespan in a temperature-dependent manner.

Accelerated age-induced nuclear morphology deterioration in *baf-1(G12T)* mutants

Alterations in NE morphology is associated with aging in several species, including *C. elegans* (Haithcock et al. 2005; Perez-Jimenez et al. 2014) and also in human progeria syndromes (Fragoso-Luna and Askjaer 2023). We therefore investigated morphology of nuclei in hypodermal cells of wild-type and *baf-1(G12T)* animals at different ages. LMN-1 and EMR-1 endogenously tagged with GFP and mCherry (mCh), respectively, were used to visualize the NE at day 1, 6 and 8 of adulthood in worms raised at 25°C. We classified nuclei based on their morphology as previously described (Perez-Jimenez et al. 2014), except that we introduced a fourth class to describe the most irregular nuclei (see Materials and Methods). Thus, while class I nuclei have smooth, uniform NE signal, classes II-IV represent progressive deterioration of nuclear morphology. At day 1, class I represented ~35% of nuclei from wild-type worms and only

194 ~20% of nuclei from *baf-1(G12T)* mutants when evaluated with either GFP::LMN-1 or EMR-
195 1::mCh (**Figure 2A-D**; $p < 0.03$; **Supplementary Table S1**). At day 6, the number of class I nuclei
196 in all strains was very reduced so we combined class I+II. Whereas class I+II represented ~90%
197 of nuclei from wild-type worms at day 1, at day 6, this fraction was reduced to 27% according to
198 GFP::LMN-1 (**Figure 2A, B**) and 42% according to EMR-1::mCh (**Figure 2C, D**). The slightly more
199 deteriorated morphology in animals expressing GFP::LMN-1 compared to EMR-1::mCh
200 suggested that tagging of LMN-1 affects it function, as described (Bone et al. 2016)(see also
201 below). Regardless of the marker, significantly fewer class I and II nuclei and more class III and
202 IV nuclei were observed in *baf-1(G12T)* on day 6. Scoring EMR-1::mCh, class I+II nuclei decreased
203 from 42% in wild-type animals to 8% in *baf-1(G12T)* mutants (**FIG 2D**; $p < 2.2e^{-16}$; **Supplementary**
204 **Table S1**). Similarly, the frequency of class IV nuclei based on GFP::LMN-1 localization increased
205 from 10% in control animals to 23% in *baf-1(G12T)* mutants (**Figure 2B**; $p = 0.0004$;
206 **Supplementary Table S1**). We also evaluated nuclear morphology after 8 days of adulthood at
207 25°C, which confirmed an increased deterioration in *baf-1(G12T)* with both NE markers
208 (**Supplementary Figure S4; Supplementary Table S1**). We concluded that alterations in nuclear
209 morphology are significantly accelerated in *baf-1(G12T)* mutants at 25°C.

210 **Nuclear envelope accumulation of lamin and emerin is reduced by the *baf-1(G12T)* mutation**

211 The amino acid residue mutated in NGPS patients is positioned close to the interface between
212 BAF and lamin (Samson et al. 2018) and experimental evidence indicates that the interaction
213 between the two proteins is weakened by the mutation (Janssen et al. 2022). However, another
214 study suggested that the interaction was unaffected (Paquet et al. 2014). Because the
215 localization of BAF and lamins are interdependent (Margalit et al. 2005), impaired interaction
216 could drive reduced BAF-1 and lamin accumulation at the NE. To test the impact of baf-1(G12T)
217 on LMN-1, EMR-1, and BAF-1 localization *in vivo*, we quantified these factors at the NE of
218 hypodermal cells. We observed an increased variation and significantly lower median GFP::LMN-
219 1 signal at the NE in *baf-1(G12T)* mutants, whereas the signal was unaffected in the nucleoplasm
220 (**Figure 2E**). Similarly, accumulation of EMR-1 at the NE was diminished by the *baf-1(G12T)*
221 mutation (**Figure 2F**). In human NGPS cells, emerin was observed to be delocalized to the ER
222 (Puente et al. 2011; Janssen et al. 2022), but we detected less cytoplasmic EMR-1::mCh signal in
223 the mutant, indicating that this NGPS phenotype is not present in the *C. elegans* model. Instead,
224 our data suggest that EMR-1 might have reduced expression when *baf-1* is mutated (see below).

225 Surprisingly, we found that the combination of *baf-1(G12T)* with the endogenously tagged
226 *gfp::lmn-1* allele *(yc32)* led to a fully penetrant maternal effect lethal (*mel*) phenotype:
227 homozygous *lmn-1(yc32[gfp::lmn-1]); baf-1(G12T)* embryos produced by hermaphrodites
228 heterozygous for the *yc32* allele developed all into adults that laid dead eggs at 20°C (**Figure 3A**).
229 We ruled out the possibility that the lethality was due to an unknown mutation in the genetic
230 background of the *yc32* allele by using a different endogenous *gfp::lmn-1* allele (*jf98*), which also
231 produced a 100% *mel* phenotype (**Supplementary Figure S5A**). In both cases, one copy of the
232 wildtype *lmn-1* allele was sufficient to sustain normal development.

233 To determine the subcellular defects that could explain the lethality of the allelic combination
234 *lmn-1(yc32[gfp::lmn-1]); baf-1(G12T)*, we recorded embryos by confocal 4D microscopy.
235 Chromosomes were visualized by co-expression of mCh::HIS-58, which revealed segregation
236 defects in early mitotic divisions and developmental arrest around 4-5h post-fertilization
237 (**Supplementary Figure S5B**). The early chromosome segregation defects prompted us to
238 investigate the embryos with higher temporal resolution. This uncovered abnormal pronuclear
239 appearance, incomplete sealing of the NE after mitosis and frequent chromosome bridges (6/10
240 embryos), which potentially is the primary cause to the observed lethality (**Figure 3B;**
241 **Supplementary Video S1**). Moreover, cell divisions were delayed (compare AB anaphase and P1
242 metaphase at 1049 sec in the control embryo versus 1149 sec in the *baf-1(G12T)* embryo).

243 Next, we analyzed endogenously tagged *gfp::baf-1* and *gfp::baf-1(G12T)* nematodes. Strikingly,
244 whereas >99% of eggs laid by homozygous *gfp::baf-1* hermaphrodites developed and hatched,
245 all eggs laid by homozygous *gfp::baf-1(G12T)* hermaphrodites (derived from balanced,
246 heterozygous hermaphrodites) were inviable (**Figure 3C**). Similarly to the *lmn-1(yc32[gfp::lmn-*
247 *1]); baf-1(G12T)* embryos, the *gfp::baf-1(G12T)* embryos arrested before elongation
248 (**Supplementary Figure S6A**). Pronuclear appearance was severely affected and, in most
249 embryos, the two pronuclei failed to juxtapose prior to the first division (**Figure 3D;**
250 **Supplementary Video S2**; 4/7 embryos). Chromosome segregation and postmitotic nuclear
251 reformation were abnormal in all *gfp::baf-1(G12T)* embryos, presumably being causative for the
252 early developmental arrest. Cell division delays were also evident in all mutant embryos.

253 Finally, we compared GFP::BAF-1 and GFP::BAF-1(G12T) expression in adults and found that
254 both proteins accumulated at the nuclear periphery in all somatic cells and in the germ line
255 (**Supplementary Figure S6B**). Quantifying the intensity at the NE or in the nucleoplasm of
256 hypodermal cells did not demonstrate any difference between wild-type and mutant BAF-1
257 (**Figure 3E**). A small reduction in cytoplasmic signal was observed for BAF-1(G12T), however, no
258 difference was detected in the ratio between nucleoplasmic/cytoplasmic signal (**Figure 3E**).
259 Taken together, our results are compatible with a model in which mutation of residue 12 of BAF
260 reduces the affinity for lamin, leading to a mild reduction in the accumulation of lamin as well
261 as emerin at the NE. Moreover, the mutation sensitizes BAF so tagging of either BAF-1(G12T) or
262 lamin with GFP has detrimental effects on chromosome segregation and NE assembly.

263 **The DNA binding profile of BAF-1 is modified by the G12T mutation**

264 BAF binds DNA *in vitro* without sequence specificity, and due to its location at the NE BAF has
265 been proposed to regulate chromatin organization (Zheng et al. 2000; Kind and van Steensel
266 2014). Moreover, human BAF A12T has been described to have altered DNA binding capacity
267 (Paquet et al. 2014), although others have disputed this claim (Marcelot et al. 2021). We decided
268 to test whether wild-type and mutant BAF-1 have different chromatin association profiles.
269 Because chromatin organization differs between tissues, subtle changes in chromatin
270 association of BAF-1(G12T) might not be detectable if averaging across multiple tissues. We
271 therefore performed tissue-specific DamID (DNA Adenine Methyltransferase Identification) by
272 expressing trace amounts of either Dam::BAF-1 or Dam::BAF-1(G12T) in two different tissues
273 using a FLP-FRT system (Munoz-Jimenez et al. 2017; Cabianca et al. 2019). We focused on the
274 hypodermis and the intestine because of skin atrophy and decreased subcutaneous fat in NGPS
275 patients (Cabanillas et al. 2011; Fisher et al. 2020).

276 DamID relies on the expression of the protein of interest fused to the DNA adenine
277 methyltransferase (Dam) of *Escherichia coli*. When the protein of interest binds chromatin, Dam
278 methylates GATC sites in close vicinity, which subsequently are identified through a series of
279 enzymatic reactions and deep sequencing (de la Cruz Ruiz et al. 2022). To normalize for
280 variations in chromatin accessibility, standard DamID protocols include a parallel sample based
281 on expression of Dam alone or Dam fused to a protein with no affinity for chromatin, such as
282 GFP. Thus, DamID can provide information about both chromatin accessibility and specific
283 binding profiles in the same experiment.

284 We first determined chromatin accessibility in L4 larvae from biological triplicates by binning
285 reads to 2kb bins (**Supplementary Figure S7A, B**). We identified 1924 bins with increased
286 accessibility in the hypodermis versus the intestine (3.8% of genome; FDR < 0.05) and 174 bins
287 with increased accessibility in the intestine (0.35% of genome). Examples of differential
288 accessibility include the genes *mua-6* and *dod-3*, which are expressed and more accessible in
289 hypodermis and intestine, respectively (**Figure 4A**). In contrast, we did not find evidence for
290 alterations in chromatin accessibility when comparing wild-type and *baf-1(G12T)* nematodes
291 and correlations were higher between the two genotypes within each replica than among

292 replicas of the same genotype (**Supplementary Figure S7A**). This suggests that BAF-1 does not
293 regulate compaction of interphase chromatin or that the mutation of residue 12 does not affect
294 this function.

295 We next calculated the log2 ratios between either Dam::BAF-1 or Dam::BAF-1(G12T) and
296 GFP::Dam to determine the binding profiles of BAF-1 and BAF-1(G12T). To visualize the global
297 distribution of the two proteins, the genome was binned into 100 kb windows. This revealed an
298 arm-center-arm pattern, where frequent association to BAF-1 or BAF-1(G12T) was detected in
299 the distal thirds of all autosomes but not in the central parts (**Supplementary Figure S8B**). The
300 pattern was highly similar between the two tissues, with few exceptions, such as the left arms
301 of chrIII and chrIV. Comparing the log2 values across all samples showed that the two tissues are
302 more dissimilar than BAF-1 and BAF-1(G12T) within each tissue (**Supplementary Figure S8A**).
303 The arm-center-arm pattern has been reported for other NE proteins, including LMN-1, EMR-1
304 and LEM-2 at different developmental stages (Ikegami et al. 2010; Towbin et al. 2012; Gonzalez-
305 Aguilera et al. 2014), as well as for the heterochromatin mark H3K9me (histone H3 methylated
306 on lysine 9) (Gerstein et al. 2010).

307 By increasing the resolution to 10 kb bins, we observed more continuous interaction of BAF-1
308 and BAF-1(G12T) on autosome arms in hypodermis versus intestine (**Figure 4B, C**). The G12T
309 mutation produced a small increase in association in chromosome centers specifically in the
310 hypodermis. We next identified bins significantly enriched for BAF-1 or BAF-1(G12T) association
311 and selected those for which the difference in log2 value between BAF-1 and BAF-1(G12T) was
312 >0.58 (equal to a fold change of 1.5). For BAF-1 in hypodermis, 410 bins on autosomes (5%)
313 fulfilled this criterium and the vast majority (87%) were located in arms (**Supplementary Table**
314 **S2**; $p < 2.2e^{-16}$). In contrast, for BAF-1(G12T) in hypodermis, enrichment was mostly observed in
315 chromosome centers (**Supplementary Table S2**; 478 enriched bins; $p = 5.0e^{-10}$). More bins were
316 differentially associated with BAF-1 or BAF-1(G12T) in intestine compared to hypodermis, but
317 they were more evenly distributed. We concluded that both BAF-1 and BAF-1(G12T) bound
318 predominantly to heterochromatin-enriched chromosome arms and that regions with subtle but
319 significant association to BAF-1(G12T) were also detected in chromosome centers in the
320 hypodermis.

321 **BAF-1(G12T) differential gene association**

322 Analysis at 2 kb bin and "gene level" (see Materials and Methods) enabled identification of genes
323 bound in the two tissues. Genome browser views illustrated again higher similarity between
324 BAF-1 and BAF-1(G12T) within tissues than either protein between tissues (**Supplementary**
325 **Figure S8C**). Nevertheless, many bins were predominantly bound by either wild-type or mutant
326 BAF-1 (**Figure 4D; Supplementary Figure S8C**). In the hypodermis, we identified 5,467 protein
327 coding and non-coding genes bound by BAF-1 and 6,376 genes bound by BAF-1(G12T)
328 (**Supplementary Table S3**). 4,541 genes (62%) associated with both proteins, whereas 2,761
329 genes (38%) are specific to either wild-type (926) or mutant (1,835) BAF-1 (**Figure 4E**). In the
330 intestine, 8,442 genes and 7,412 genes were bound by BAF-1 and BAF-1(G12T), respectively. Of
331 these, 5,410 genes (51%) were identified in both datasets, whereas 3,032 genes (29%)
332 associated specifically with BAF-1 and 2,078 genes (20%) specifically with BAF-1(G12T) (**Figure**
333 **4E**). Comparing all 4 datasets, 8,056 genes (62%) are present in at least two datasets whereas
334 4,839 genes (38%) are unique; 2,552 genes (20%) are bound by wild-type and mutant BAF-1 in
335 both tissues (**Supplementary Table S3**).

336 Analyzing the BAF-1 and BAF-1(G12T)-bound genes for tissue enrichment (Angeles-Albores et al.
337 2016) retrieved the categories *Nervous system*, *Epithelial system*, *Male*, and *Amphid sheath cell*
338 in both hypodermis and intestine and by both wild-type and mutant BAF-1 (**Figure 4F;**
339 **Supplementary Table S3**). In contrast, the categories *Reproductive system*, *Germ line*, and *Male*
340 *distal tip* were enriched for binding to wild-type BAF-1, but not BAF-1(G12T) in the hypodermis

341 (**Figure 4F**). For all these categories, except *Epithelial system*, genes are generally inactive in the
342 two tissues that we analyzed. This suggested that BAF-1 binding correlates inversely with gene
343 expression (see Discussion regarding the *Epithelial system*).

344 **Deregulation of ribosomal and cuticle genes in *baf-1(G12T)* mutants**

345 We next used tissue-specific RNA polymerase DamID (RAPID) (Gomez-Saldivar et al. 2020;
346 Fragoso-Luna et al. 2023) to identify genes expressed in hypodermis and intestine in wild-type
347 and *baf-1(G12T)* mutants. In wild-type animals, 1,960 genes were detected as expressed in
348 hypodermis and 1,585 genes in intestine (**Supplementary Table S4**). Of these, 491 genes were
349 shared between the two tissues. To explore if association to BAF-1 correlates with expression,
350 we calculated the median and average log2(Dam::BAF-1/GFP::Dam) values for genes expressed
351 in both tissues, in only one of them or in neither. In the hypodermis, we found that the log2
352 values were lowest for genes expressed in this tissue, whereas genes expressed in intestine had
353 intermediate values (**Figure 5A**). A similar picture emerged when analyzing genes expressed only
354 intestine (**Figure 5B**). These data suggest that expressed genes are generally depleted for
355 interaction with BAF-1.

356 By comparing hypodermal RAPID scores between wild-type and *baf-1(G12T)* we identified 36
357 genes that were reproducibly upregulated in the mutant and 26 genes that were downregulated
358 (**Figure 5C**; **Supplementary Table S4**). More genes were deregulated in the intestine with 76
359 genes being more expressed in *baf-1(G12T)* and 53 genes being repressed (**Figure 5D**;
360 **Supplementary Table S4**). Although only 0.9-2.5% of expressed genes in the two tissues were
361 deregulated, gene ontology (GO) analysis revealed a significant overrepresentation of several
362 GO terms. Genes related to histone acetylation, proton transport and ribosomes were
363 deregulated in both tissues, whereas other classes appeared only in hypodermis (e.g. cuticle
364 components) or intestine (**Figure 5E**).

365 Although we found that expressed genes are generally devoid of interaction with BAF-1, we
366 speculated that the deregulation of the genes identified in our RAPID experiments could be
367 related to altered BAF-1 binding. We plotted the DamID scores obtained with Dam::BAF-1(G12T)
368 versus Dam::BAF-1 for the deregulated genes, focusing initially on the intestine because of the
369 higher number of deregulated genes. The majority of deregulated genes had negative log2
370 scores, implying more frequent interaction with GFP::Dam than with either Dam::BAF-1 or BAF-
371 1(G12T). Surprisingly, both upregulated (**Figure 6A**) and downregulated (**Figure 6B**) genes had
372 higher log2 scores for BAF-1(G12T) compared to the wild-type protein. This result indicates that
373 deregulated genes are bound more often when BAF-1 it mutated. Two exceptions appeared
374 among the downregulated genes: F14E5.8 (an uncharacterized protein with no obvious ortholog
375 in vertebrates) and *emr-1*, which both were bound by BAF-1 but not BAF-1(G12T) (**Figure 6B**).
376 Whether BAF-1 is involved in activation of these genes remains to be tested. We also noted that
377 among the 129 deregulated genes in the intestine, 13 encode ribosomal proteins (Q value = $2.4e^{-}$
378 ^{9}). Strikingly, all 5 upregulated and 7/8 downregulated ribosomal genes had higher log2 scores
379 with BAF-1(G12T) than with BAF-1 (**Figure 6A-C**; p = 0.0009). The genes that were deregulated
380 in the hypodermis showed little difference in their interaction with the two versions of BAF-1
381 (**Supplementary Figure S9A, B**). However, genes encoding cuticle constituents were
382 overrepresented (8/62 genes, Q value = $1.2e^{-6}$) and 7 of these showed decreased interaction
383 with BAF-1(G12T) compared to BAF-1 (**Supplementary Figure S9C**; p = 0.03). Thus, although
384 there is no uniform correlation between changes in association to BAF-1 and changes in gene
385 expression, several gene classes appear to have specific behaviors.

386 **BAF-1(G12T) induces alterations in stress resistance**

387 Cells derived from HGPS patients suffer chronic oxidative stress and stimulation of antioxidant
388 pathways can reverse cellular HGPS phenotypes (Kubben et al. 2016). Because of the similarities
389 between NGPS and HGPS, we speculated that *baf-1(G12T)* mutants might be hypersensitive to

390 oxidative stress. Surprisingly, we observed that *baf-1(G12T)* mutants survived longer than
391 control animals upon exposure to tert-butyl hydroperoxide (**Figure 7A**; $p < 2e^{-16}$). Based on this
392 result, we tested if the *baf-1(G12T)* mutants displayed changes in resistance to other systemic
393 stressors. Gene ontology analysis suggested an enrichment in genes involved in *Response to X-*
394 *ray baf-1(G12T)* mutants. We therefore exposed young adults to DNA damaging ultraviolet light
395 and scored survival in the progeny. *baf-1(G12T)* mutants exhibited reduced survival in 7/8
396 samples (**Figure 7B**; p = 0.04), indicating that the ability to repair UV-induced DNA damage is
397 compromised by the NGPS mutation. We next tested the response to acute heat stress, which
398 provokes protein misfolding and aggregation and consequently activation of several response
399 pathways, such as heat shock response, unfolded protein response and autophagy. When
400 incubated at 35°C, the median survival of control hermaphrodites was 6 h versus 5 h for *baf-*
401 *1(G12T)* mutants (**Figure 7C**; p = 0.00001). Thus, mutation of BAF-1 led to significantly reduced
402 heat stress resistance and further studies should determine which response pathway(s) is
403 impaired. We concluded that the NGPS mutation causes increased sensitivity to certain stress
404 factors, but also that the mutation can protect against oxidative stress, which contrasts the
405 situation in HGPS.

406

407 **DISCUSSION**

408 The need for a deeper understanding of healthy aging is becoming increasingly important, as
409 the life expectancy of the world population has augmented in the last century. Studies on
410 accelerating aging diseases have provided insight on different pathways that are altered during
411 physiological aging, but specific mechanisms underlying these conditions have also emerged.
412 The use of animal models is an instrumental source of knowledge due to the possibility of
413 studying the effect of mutations and interventions at multiple scales. In this study, we
414 established *C. elegans* as a model to study how a progeria-causing mutation in BAF affects
415 nuclear organization, gene expression and physiology. Our work has provided insight not only
416 to the differences in chromatin association between wild-type and mutant BAF-1 but also on
417 tissue-specific interactions of BAF-1 with predominantly silent genes. The observation that
418 nuclear morphology deteriorated faster in *baf-1(G12T)* mutants argues that *C. elegans* is a
419 relevant model to investigate NGPS. Importantly, the differential sensitivities to irradiation,
420 temperature and oxidative stress suggest a complex organismal response to the G12T
421 substitution in BAF-1 and warrant further investigation. Recently, *Drosophila* was reported as
422 another invertebrate NGPS model, which revealed defects in centromere function and ovary
423 homeostasis (Duan et al. 2023). We anticipate that these two relatively simple animal models
424 will provide important platforms for both discovery and validation of potential targets and
425 treatments.

426 NGPS patient-derived fibroblasts exhibits partial delocalization of emerin from the NE to the
427 cytoplasm (Puente et al. 2011; Janssen et al. 2022). Although we observed a mild but significant
428 decrease in NE accumulation of EMR-1, we did not see an increase in cytoplasmic EMR-1 levels.
429 The behavior of emerin in the *Drosophila* NGPS model (Duan et al. 2023) was like the situation
430 in *C. elegans*, suggesting that emerin might be affected by the NGPS mutation in a species and/or
431 cell type-specific manner, for instance due to the presence or absence of other interaction
432 partners. NE accumulation of LMN-1 was also reduced in *baf-1(G12T)* mutants, which is
433 compatible with a model in which 1) lamin depends on BAF to localize at the NE (Margalit et al.
434 2005) and 2) the affinity of BAF for lamin is reduced by the NGPS mutation (Samson et al. 2018;
435 Janssen et al. 2022). We found that localization of BAF-1 itself was unaffected in the NE of *C.*
436 *elegans* somatic and germline tissues. This result contrasts with observations in flies, where the
437 NGPS mutation led to reduced NE accumulation (Duan et al. 2023). Different behaviors of BAF
438 A12T in human cells have been reported: ectopic expression showed in one study no difference
439 in the accumulation of wild-type and mutant BAF at the NE (Paquet et al. 2014), whereas another

440 study concluded that NE accumulation of BAF A12T was impaired (Puente et al. 2011). Finally,
441 using antibodies to compare endogenous BAF localization in control and NGPS fibroblasts found
442 a reduced nucleocytoplasmic ratio in the latter (Janssen et al. 2022).

443 Tagging BAF-1 and BAF-1(G12T) endogenously with GFP revealed a striking difference during
444 early development. Whereas tagging of wild-type BAF-1 had no obvious effect on fitness at any
445 stage of development, *gfp::baf-1(G12T)* embryos suffered severe nuclear appearance and
446 chromosome segregation defects already from the 1 cell-stage and all died before hatching. This
447 was in stark contrast with the ~100% viability of untagged *baf-1(G12T)* embryos. Surprisingly,
448 endogenous GFP tagging of LMN-1 also caused a fully penetrant embryonic lethal phenotype
449 when combined with the *baf-1(G12T)* allele. This lethality seemed specific to LMN-1 because
450 *emr-1::mCh; baf-1(G12T)* individuals developed normally. Moreover, timelapse recordings
451 unraveled similar defects in early *gfp::baf-1(G12T)* and *gfp::lmn-1; baf-1(G12T)* embryos. One
452 possible explanation is that GFP physically interferes with the interaction between BAF-1 and
453 LMN-1 and that this is only critical when BAF-1 carries the G12T mutation. Steric hindrance can
454 be envisioned both in the case of N-terminal tagging of BAF-1 because of proximity of BAF's N
455 terminus to the BAF·lamin interface, and in the case of N-terminal tagging of LMN-1 because
456 lamin dimers form head-to-tail polymers where the BAF-interacting globular domain of lamin
457 might be in proximity with the N terminus of the neighboring lamin molecule (Turgay et al. 2017;
458 Samson et al. 2018). In support of this hypothesis, animals with endogenously tagged LMN-1
459 and EMR-1 (*gfp::lmn-1; emr-1::mCh*) were fully viable, whereas we could not create a strain that
460 was homozygous for endogenous GFP::LMN-1 and mCh::BAF-1 (data not shown). We conclude
461 that insertion of fluorescent tags has a dramatic effect in *baf-1(G12T)* nematodes as well as in
462 flies (Duan et al. 2023). Although further studies are needed to determine the molecular
463 mechanism, we note that the high lethality of *gfp::lmn-1; baf-1(G12T)* embryos provides an ideal
464 sensitized genetic background to screen for suppressors (Breusegem et al. 2022).

465 Tissue-specific DamID unveiled that BAF-1 bound predominantly to the distal arms of
466 chromosomes, which are characterized by accumulation of repetitive elements and
467 heterochromatin marks, in particular methylation of histone H3 on lysine 9 (Gerstein et al. 2010;
468 Ahringer and Gasser 2018). In accordance with BAF-1's direct interactions with LMN-1, EMR-1
469 and LEM-2, DamID and chromatin immunoprecipitation profiles of these three proteins also
470 show enrichment in chromosome arms (Ikegami et al. 2010; Towbin et al. 2012; Gonzalez-
471 Aguilera et al. 2014). Although the profiles of BAF-1 in hypodermis and intestine overlapped
472 closely throughout most of the genome, we also detected regions larger than 100 kb that only
473 interacted with BAF-1 in one of the tissues. At the level of individual genes, we found that
474 expressed genes identified in our tissue-specific RAPID experiments were largely devoid of
475 interaction with BAF-1. Although this was expected, based on the trend that genes positioned
476 at the nuclear periphery are often transcriptionally silent (Ahringer and Gasser 2018; Manzo et
477 al. 2022), our study represents the first mapping of BAF binding sites at gene resolution in any
478 species. We observed an enrichment of BAF-1 at genes related to the nervous system and male-
479 specific structures both in hypodermis and intestine where these genes are mostly silent. The
480 appearance of the category *Epithelial system* as enriched for BAF-1 binding in hypodermis and
481 intestine was surprising because we expected genes in this category to be expressed in these
482 tissues. However, *Epithelial system* encompasses several thousand genes and inspection of the
483 BAF-1-bound genes in this category revealed that <3% were detected as expressed in the
484 hypodermis in our RAPID experiments or in another recent hypodermal transcriptomic dataset
485 (Katsanos et al. 2021) (data not shown). We therefore concluded that BAF-1 binding in general
486 correlates inversely with gene expression.

487 On a global scale, the chromatin association profile of BAF-1 and BAF-1(G12T) were highly
488 similar, indicating that the NGPS mutation does not provoke chromosome repositioning.
489 However, many changes were observed at the level of a few kb. In each of the two tissues, BAF-

1 and BAF-1(G12T) bound 7,302-10,520 protein coding and non-coding genes (16-23% of all genes). More than half of the genes (51-62%) were shared between the wild-type and the mutant protein, whereas the number of uniquely bound genes ranged from 926 to 3,032 (13-29%). In the hypodermis, the different binding profiles manifested in several tissue enrichment analysis terms appearing only with wild-type BAF-1 (*Reproductive system*, *Germ line*, and *Male distal tip*). Despite the large number of genes that showed differences in association to BAF-1 versus BAF-1(G12T), relatively few genes were detected as deregulated. DamID-based methods, such as RAPID and TaDa, use RNA polymerase occupancy as a reliable proxy for gene expression (Southall et al. 2013; Gomez-Saldivar et al. 2020; Katsanos et al. 2021). However, subtle changes in transcription might not be detectable. Among the deregulated genes, several were related to metabolic processes (e.g. *Proton transport, ATP generation*, *Mitochondrial protein import*, etc.) and chromatin regulation (*Histone acetylation*). The most frequent deregulated genes were *Cuticle components* in the hypodermis and *Ribosome components* in both tissues. Seven of the eight deregulated cuticle genes in the hypodermis associated less frequently with BAF-1(G12T) than with BAF-1. For ribosomal genes the correlation was even more pronounced and in the opposite direction: 12 of the 13 deregulated ribosomal genes in the intestine associated less frequently with BAF-1(G12T) than with BAF-1. Surprisingly, in the intestine, both upregulated and downregulated genes bound more frequently to the mutant BAF-1 protein. The genes that changed both association with BAF-1 and expression level in the context of the G12T mutation might represent primary NGPS alterations. Importantly, translation levels and fidelity were observed to be altered in NGPS fibroblasts and depletion of ribosome components could improve several cellular parameters (Breusegem et al. 2022).

Limited information is available on fertility in progeria patients (Donadille et al. 2013), but mutations in components of the NE LINC (linker of nucleoskeleton and cytoskeleton) complex cause infertility in several animal species (Link and Jantsch 2019). We observed a strong reduction in brood size of *baf-1(G12T)* hermaphrodites at 25°C, which at least in part could be ascribed to a diminished presence of sperm in the spermatheca. Sperm production in hermaphrodites occurs during the L4 stage. The observation that the brood size phenotype depended on incubation at 25°C during L4 stage or before points towards sperm-related defects. Moreover, more than one third of the oocytes that passed through the spermatheca of *baf-1(G12T)* hermaphrodites on day 1 of adulthood were not fertilized, despite sperm still being present. This fertility defect was rescued by mating with wild-type males, suggesting that *baf-1(G12T)* sperm were abnormal but oocytes unaffected. Mating feminized worms to *baf-1(G12T)* males produced significantly fewer progeny compared to *fog-2* males, suggesting *baf-1(G12T)* also causes defective male in sperm. Sperm, in contrast to oocytes, lack a typical nuclear membrane. Instead, a halo on undefined composition encapsulates sperm DNA, RNA, and centrioles (Wolf et al. 1978). In this study, we found that BAF-1 but neither LMN-1 nor EMR-1 was present in mature sperm in adults of both sexes. Moreover, the *baf-1(G12T)* mutation did not alter this behavior. It is therefore possible that BAF-1 has a specific role in spermatogenesis that is affected by the NGPS mutation, but further studies are required to explore this.

Stress resistance correlates positively with longevity, whereas alterations in stress response pathways are intrinsically linked to diseases (Soo et al. 2023). In this context, we consider the reduced resistance of *baf-1(G12T)* mutants to temperature stress and UV irradiation reported in this study as a reflection of an overall impaired health span. We envision that they can be explored as traits in future experiments designed to identify genes or compounds that improve the health of *baf-1(G12T)* nematodes. However, the *baf-1(G12T)* mutation increased resistance to oxidative stress, highlighting the complex interplay between different stress response pathways and the need to evaluate potential interventions in multiple conditions to minimize negative side effects. In this aspect, invertebrate models, like nematodes and flies, are very attractive due to easy manipulation, low cost, and fast generation times (Yamamoto et al. 2024).

540 In conclusion, we have characterized the effect of introducing in *C. elegans* a mutation described
541 to cause NGPS in humans. Our results support the proposal that the NGPS mutation induces
542 changes in BAF's interaction with lamin and they are also consistent with the hypothesis that
543 the mutation alters BAF's affinity for chromatin. Importantly, *baf-1(G12T)* mutants reproduce
544 several progeria phenotypes, including reduced lifespan, accelerated nuclear deterioration,
545 lower fertility and altered stress resistance. We propose that these characteristics make *C.*
546 *elegans* a relevant model to study the molecular mechanisms of NGPS and to explore possible
547 interventions. Hopefully, combining the advantages of a simple *in vivo* model with those of
548 human cell and organoid cultures will lead to the discovery of efficient therapies.

549

550 **MATERIALS AND METHODS**

551 **Nematode strains and transgenesis**

552 Strains were maintained at 16°C or 20°C on Nematode Growth Medium (NGM) petri dishes
553 seeded with *Escherichia coli* OP50 using standard *C. elegans* methods (Stiernagle 2006). New
554 strains were generated by MosSCI (Frøkjær-Jensen et al. 2012; Dobrzynska et al. 2016a),
555 CRISPR/Cas9 (Arribere et al. 2014; Paix et al. 2015; Schwartz and Jorgensen 2016) and crossing
556 of existing strains. Descriptions and genotypes of all strains are listed in **Supplementary Table**
557 **S5**. The N2 strain was used as wild-type reference.

558 **Molecular cloning**

559 Plasmids pBN296 *hsp16.41p>mCh::his-58>dam::baf-1* and pBN298 *hsp16.41p>mCh::his-*
560 *58>dam::baf-1(G12T)* for DamID were constructed by amplifying *baf-1* and *baf-1(G12T)* with
561 primers B925 and B926 (see primer sequences in **Supplementary Table S6**) using genomic DNA
562 as template. The PCR product was digested with BglII and NheI and inserted into plasmid
563 pBN209 *hsp16.41p>mCh::his-58>dam::emr-1* (Cabianca et al. 2019) digested with the same
564 enzymes to replace *emr-1*.

565 Plasmid pBN566 *emr-1p::emr-1::mCh* with Frt sites in the first introns of *emr-1* and mCh was
566 made by insertion of a synthetic gBlock B840 into plasmid pBN20 (Morales-Martinez et al. 2015),
567 which contains 1568 bp upstream of the *emr-1* start codon, the *emr-1* CDS, mCh and 301 bp
568 downstream of the *emr-1* stop codon.

569 Plasmid pBN180 to insert and express sgRNAs from the promoter of R07E5.16
570 (WBGene00014484) was derived from pDD162 (Dickinson et al. 2013) by whole-plasmid PCR
571 with NEB Q5 polymerase and primers B633 and B634, deleting the Cas9 cassette. Plasmid
572 pBN180 was further modified by whole-plasmid PCR with primers B780 and B781 to generate
573 pBN215 that enables expression of sgRNA(E+F) (Ward 2015). Plasmids pBN207, pBN240 and
574 pBN485 to express sgRNAs corresponding to *dpy-10*, *emr-1* 3'-end and *emr-1* 5'-end,
575 respectively, were generated by whole-plasmid PCR with primer B635 and either primer B724
576 (*dpy-10*), B825 (*emr-1* 3'-end) or B838 (*emr-1* 5'-end) using either pBN180 (*dpy-10*) or pBN215
577 (*emr-1*) as PCR template. All DNA oligonucleotides were purchased from IDT.

578 **CRISPR/Cas9 genome editing**

579 Strain BN1007 *+/mT1 [umnIs34] II; baf-1(bq24[G>F>P::baf-1[G12T]])/mT1 [dpy-10(e128)] III* was
580 generated by microinjection of targeting plasmid pBN313 (Munoz-Jimenez et al. 2017) at 65
581 ng/µl into the gonads of BN868 *baf-1(bq19[G12T]) unc-119(ed3) III* young adult hermaphrodites
582 together with plasmids #1286 *eft-3p::Cas9* ((Friedland et al. 2013); 25 ng/µl), pBN1 *lmn-*
583 *1p::mCh::his-58* ((Rodenas et al. 2012); 10 ng/µl), pCFJ90 *myo-2p::mCh* ((Frøkjær-Jensen et al.
584 2008); 2.5 ng/µl) and pCFJ104 *myo-3p::mCh* ((Frøkjær-Jensen et al. 2008); 5 ng/µl). Successful
585 modification of the *baf-1(G12T)* locus was confirmed by detection of fluorescent fusion protein
586 in the NE, absence of ectopic mCherry expression from the co-injection markers and Sanger

587 sequencing. The *unc-119(+)* selection marker was next excised by microinjection with Cre
588 expression plasmid pMLS328 (Schwartz and Jorgensen 2016). Finally, uncoordinated
589 hermaphrodites were outcrossed to N2 males to remove the *unc-119(ed3)* allele and balanced
590 with mT1.

591 Strain BN1024 *emr-1(bq34[emr-1::mCh]) I* was generated by microinjection of repair template
592 plasmid pBN566 at 50 ng/µl into the gonads of N2 young adult hermaphrodites together with
593 plasmid #1286 *eft-3p::Cas9* (50 ng/µl), sgRNA plasmids (pBN207, pBN240 and pBN485; 25 ng/µl
594 each) and *dpy-10* single-stranded repair template B725 (500 nM). Successful modification of the
595 *emr-1(G12T)* locus was confirmed by detection of fluorescent fusion protein in the NE and
596 Sanger sequencing followed by outcrossing twice to N2.

597 Strain PMX375 was generated by CRISPR-mediated gene editing, introducing the mutation
598 c.34_35GG>AC into the endogenous *baf-1* locus, and then six times outcrossed to N2, to
599 eventually produce the strain BN808 *baf-1(bq19[G12T]) III*.

600 **Mos1-mediated single-copy integration**

601 Single-copy insertion of tissue-specific DamID constructs into the *ttTi5605* locus on chrII was
602 done by microinjection into the gonads of EG4322 young adult hermaphrodites. Plasmids
603 pBN296 and pBN298 carrying *unc-119(+)* as selection marker were injected at 50 ng/µl together
604 with pCFJ601 *eft-3p::Mos1* ((Frøkjær-Jensen et al. 2012), 50 ng/µl), pBN1 (10 ng/µl), pCFJ90 (2.5
605 ng/µl) and pCFJ104 (5 ng/µl). Integration of the constructs was confirmed by PCR and heat-
606 inducible expression of mCh::HIS-58.

607 **Lifespan assay**

608 Lifespan assays were performed as described (Haithcock *et al.* 2005). Animals were examined
609 every 1–3 days and transferred to fresh plates every day for the first 5 days and then every 5–7
610 days. For experiments involving RNA interference (RNAi), plates contained 1 mM IPTG and 25
611 µg/ml ampicillin were seeded with 100 µl of *E. coli* HT115 bacterial culture the previous day.
612 Control and *daf-16* RNAi proceeded from the Ahringer RNAi library (Kamath et al. 2003). Animals
613 that crawled off the plate or displayed extruded internal organs or internal hatching were
614 censored. Animals were considered dead when they failed to respond to gentle touch. Kaplan–
615 Meir curves were prepared and analyzed with R (R version 3.6.3) and R Studio (Version 1.1.463;
616 (Team 2020)). All experiments were performed at least in triplicate and combined, except the
617 results represented in Supplementary Figure S1D. Statistical analysis was performed by using
618 the R package survival that provides the chi-square statistic for a test of equality.

619 **Brood size assay**

620 Three to five L4 worms per strain and per replica were individually picked on NGM plates seeded
621 with *E. coli* OP50 and changed every 24 hours until eggs laying ceased. Parental animal that
622 crawled off the plate, dug into the agar, or suffered internal hatching precociously were
623 censored. Progeny was counted after 2 days of development. All experiments were performed
624 at least by triplicate. Statistical analysis was performed with R Studio using a two-tailed t-test.

625 **Nuclear morphology assay**

626 Three to five hermaphrodites per genotype grown at 25°C since L4 were observed at days 1, 6
627 and 8 after reaching L4 on each replica. Animals were anaesthetized with 10 mM levamisole and
628 mounted on thin 2 % agarose pads (de la Cruz Ruiz et al. 2022). A Nikon A1R microscope
629 equipped with a 60x objective was used to acquire confocal micrographs of hypodermal nuclei
630 every 1-2 µm from the surface of the worm to cover the entire depth of the hypodermis. Nuclear
631 morphology was classified into four groups without revealing the genotype of the specimens to
632 the researcher: class I) nuclei with uniform and smooth NE staining; class II) nuclei with
633 enhanced intranuclear staining of NE components and mildly lobulated nuclei; class III) nuclei

634 with highly irregular nuclear shape and accumulation of NE protein in bright foci concomitantly
635 with reduced peripheral signal; class IV) nuclei similar to class III but with protrusions of the NE
636 or ruptured NEs that release chromatin to the cytoplasm. All experiments were performed at
637 least by triplicate. Statistical analysis was performed by using Fisher's exact test in R Studio.

638 **Quantification of fluorescence intensity**

639 To quantify the fluorescence intensity of GFP::LMN-1, EMR-1::mCh, GFP::BAF-1 and GFP::BAF-
640 1(G12T), images of hypodermal nuclei were acquired as above and fluorescence intensity was
641 quantified with Fiji/ImageJ 2.1.0/1.53c (Schindelin et al. 2012) using the function Plot Profile of
642 a manually drawn, 5 pixel wide straight line across the entire nucleus. NE values were obtained
643 by averaging 3 consecutive values centered around the highest value on each side of the
644 nucleus. Nucleoplasm intensity values were determined by averaging consecutive 5 values from
645 the middle between the 2 NE maxima. Cytoplasm intensity values were determined by averaging
646 3 consecutive values 1 µm away from the NE on each side of the nucleus. Images of aged-
647 matched N2 worms were used as background. Statistical analysis was performed with R Studio
648 using a two-tailed t-test. Whereas quantification was performed on raw 12 bits images, identical
649 adjustment of brightness and contrast was applied to all comparable panels within each figure
650 panels.

651 **Time lapse recordings**

652 Embryos were obtained by cutting open gravid hermaphrodites using two 21-gauge needles,
653 mounted on a coverslip in 3 µl of M9 buffer. The coverslip was placed on a 2% agarose pad. For
654 high temporal resolution videos, 1 cell-stage embryos were recorded with a Yokogawa CSU-X1
655 spinning disc confocal scanning unit mounted on a Olympus IX-81 microscope equipped with
656 491 nm and 561 nm lasers and a 100x objective. Acquisition parameters were controlled by
657 MetaMorph software (v7.8.13.0). Z stack series consisting of 17 slices separated by 0.3 µm were
658 acquired every 12.5-20.4 sec followed by maximum projection for each time point. For
659 recordings of the entire embryonic development, coverslips were sealed with VALAP to avoid
660 desiccation and 5 confocal sections separated by 2 µm were acquired every 10 minutes on a
661 Nikon A1R microscope equipped with a 60x objective, Nikon Perfect Focusing System and 488
662 nm and 561 nm lasers. Single confocal sections were used for mounting figures. Room
663 temperature was 20-23°C. Images were processed using FIJI software, always applying identical
664 settings to control and mutant recordings.

665 **Resistance to ultraviolet irradiation**

666 For every replica, 12-15 L4 hermaphrodites were isolated and grown at 20°C. Next day, five of
667 these worms were transferred to a new dish an irradiated in a Hoefer UVC 500 UV Crosslinker,
668 with a dose of 25 J/m2. In parallel, another five worms were isolated but were not exposed to
669 UV. Both, irradiated and non-irradiated worms were incubated for 2 hours at 20°C. Then, after
670 removing the adults, eggs were counted, and plates were incubated at 20°C. The day after,
671 larvae and non-hatched eggs were quantified. Statistical analysis was performed with R Studio
672 using a two-tailed paired t-test.

673 **Heat stress assay**

674 L4 worms were picked the day before the assay and maintained overnight at 20°C. The day of
675 the assay, thermotolerance resistance was evaluated by transferring 20 young adults to an NGM
676 plate without bacteria and incubated in a water bath at 35°C. Viability was scored every hour
677 after 2 hours and death was determined by the lack of movement and/or pharyngeal pumping
678 after gentle prodding. The experiment was performed in triplicate and the combined data were
679 analyzed as described for lifespan above.

680 **Oxidative stress assay**

681 The animals were synchronized as L1 larvae by egg-prepping with hypochlorite (Stiernagle 2006)
682 and hatching in M9. L1 larvae were then seeded onto 6 cm NGM plates containing 1 mM IPTG
683 and 50 µg/ml carbenicillin seeded with *E. coli* HT115 (transformed with the L4440 plasmid).
684 Animals were grown at 15°C until the late L4 stage, followed by the addition of 5-Fluoro-2'-
685 deoxyuridine (50 µM final concentration) and shifted to 20°C. At day 2 of the adulthood, animals
686 were washed off the plates with M9 and transferred to plates containing 6 mM tert-butyl
687 hydroperoxide (tBOOH). Seeding density was approximately 50 animals per plate. Plates were
688 then incubated at 20°C and the animals' survival was recorded and analyzed by a fully
689 automated lifespan machine as previously described (Stroustrup et al. 2013). For each condition,
690 a minimum of 150 worms distributed over at least 4 separate plates was scored. The combined
691 data were analyzed as described for lifespan above.

692 **Bacteria culture for DamID plates**

693 *E. coli* GM119 *dam-* was grown by pre-inoculating 1-2 colonies from a fresh LB/agar plate in
694 liquid LB without antibiotics. The pre-inoculum was grown overnight at 37°C before transferring
695 1 ml of culture to a suitable volume of LB (depending on the numbers of plates to be seeded,
696 i.e. for 10 plates with a diameter of 10 cm prepare at least 10 ml culture) and incubated for 6
697 hours at 37°C. Next, 700 µl of bacteria culture was added to each 10 cm NGM plate, spread and
698 incubated overnight at 37°C.

699 **Nematode culture for DamID**

700 Worms were grown asynchronically at 20°C on NGM plates seeded with *E. coli* GM119 for at
701 least two generations before egg-prepping with hypochlorite. Hatched L1s were counted the
702 day after and 1000 L1s were aliquoted onto 10 cm NGM plates seeded with *E. coli* GM119 as
703 described above. Worms were grown at 20°C for 48 h before collecting 4000 L4 stage nematodes
704 per strain and washed 8 times with 15 ml of M9 with 0.01% Tween-20. Worms were transferred
705 to 1.5 ml tubes with M9 with 0.01% Tween-20 using Pasteur pipettes followed by two additional
706 washes. Supernatants were aspirated and aliquots of 30 µl were snap frozen in liquid nitrogen
707 and maintained at -80°C until DNA extraction.

708 **DamID amplification, library preparation and sequencing**

709 To purify genomic DNA, samples were lysed in 5 freeze/thaw cycles (1min in liquid nitrogen;
710 3min in 37C shaker) and processed with DNeasy Blood and Tissue Kit (QIAGEN #69504). DamID
711 was performed on 200-400 ng genomic DNA (gDNA; 200 ng was used for RNA polymerase DamID
712 [RAPID]; 400 ng was used for BAF-1 and BAF-1(G12T) DamID) extracted from 4000 L4 animals
713 cultured and collected as indicated above. Two (RAPID) or three (BAF-1 and BAF-1(G12T) DamID)
714 replicates were performed as described (de la Cruz Ruiz et al. 2022). For RAPID, a pool of 3 AdR
715 primers (B1436 AdR4N, B1437 AdR5N, B1438 AdR6N) and 14 PCR cycles were used. For BAF-1
716 and BAF-1(G12T) DamID we used B916 AdR and 22 PCR cycles. Successful amplification of Dam-
717 methylated genomic DNA yielded a smear of ~400-~1500 bp fragments when analyzed on
718 Agilent Bioanalyzer.

719 Either 40 ng (RAPID) or 400 ng (BAF-1 and BAF-1(G12T) DamID) of PCR amplified fragments were
720 used for library preparation as described (de la Cruz Ruiz et al. 2022), using E7370 NEBNext®
721 Ultra™ DNA Library Prep Kit for Illumina. Library amplicons' size distribution was checked to be
722 maintained as for PCR fragments indicated above followed by pooling, repurification and
723 sequencing on a Illumina NextSeq500 platform at EMBL GeneCore.

724 **Bioinformatic analysis**

725 FASTQ files from the NextSeq500 platform were processed in R Studio using the pipelines
726 RDamIDSeq (https://github.com/damidseq/RDamIDSeq) and RGeneDamIDSeq
727 (https://github.com/damidseq/-RGeneDamIDSeq-) (Sharma et al. 2016) for mapping of reads to

728 bins of fixed size (e.g. 2 kb, 10 kb or 100 kb) and to genes, respectively. The pipelines include a
729 quality check where only reads that contain the DamID adapter ("CGCGGCCGAG") and map to
730 GATC sites in the *C. elegans* genome are retained for further analysis. The number of reads
731 fulfilling these criteria ranged from 0.5 to 27 million (see **Supplementary Table S7**). Both
732 pipelines also provide mapped read numbers per individual GATC fragment. For mapping to
733 genes, the script was modified to include 500 bp distal to transcriptional start and termination
734 sites. UCSC genome version ce11 (BSgenome.Celegans.UCSC.ce11) was used for alignment.

735 For BAF-1 and BAF-1(G12T) DamID the DESeq2 package (Love et al. 2014) was used to identify
736 bins with significantly more reads with either Dam::BAF-1 or Dam::BAF-1(G12T) compared to
737 GFP::Dam across the 3 replicas. A false discovery rate (FDR) of 0.05 was used as threshold. Next,
738 for each sample a pseudocount of 1 was added to each bin and the relative number of reads per
739 bin was calculated followed by averaging across the replicas. The ratio of Dam::BAF-1 or
740 Dam::BAF-1(G12T) to GFP::Dam was calculated for each bin and log2-transformed. Finally,
741 normalization was done by subtracting the genome-wide average log2 ratio from the log2 ratio
742 of each bin (Brueckner et al. 2020).

743 For RAPID, normalization of Dam::RPB-6 reads to GFP::Dam reads was performed using the
744 damidseq_pipeline package (https://owenjm.github.io/damidseq_pipeline/) (Marshall and
745 Brand 2015) on the bam files generated by the RDamIDSeq pipeline. Gene occupancy was
746 computed as log2(Dam::RPB-6/GFP::Dam) with polii.gene.call
747 (https://github.com/owenjm/polii.gene.call) using bedgraph output files from the
748 damidseq_pipeline and WBCel235 gene annotation. A FDR of 0.05 was used as threshold to call
749 transcribed genes.

750 For comparison of chromosome centers versus heterochromatin-rich distal arms, we used the
751 following border coordinates: ChrI 3745632 and 10809938, ChrII 4708341 and 11877168, ChrIII
752 3508994 and 9947268, ChrIV 7317812 and 12176625, ChrV 8125434 and 13849337, and ChrX
753 41919362 (Gonzalez-Aguilera et al. 2014). Pairwise Wilcoxon rank test values were calculated in
754 R.

755 Genome browser views and Venn diagrams were generated with the University of California
756 Santa Cruz Genomics Institute Genome Browser (http://genome.ucsc.edu; (Kent et al. 2002))
757 and jvenn (Web App) (Bardou et al. 2014), respectively. The WormBase Enrichment Suite
758 (http://www.wormbase.org/tools/enrichment/tea/tea.cgi; (Angeles-Albores et al. 2018)) was
759 used for tissue enrichment and gene ontology analysis.

760 Raw and processed DamID files are deposited at the NCBI Gene Expression Omnibus
761 (https://www.ncbi.nlm.nih.gov/geo/).

762

763 **ACKNOWLEDGMENTS**

764 We are grateful to Marta Rojas for assistance in genetic crosses, Laura Tomás from the CABD
765 Proteomics and Biochemistry Facility for recombinant Cas9, Katherina García from the CABD
766 Imaging Facility and Ildefonso Cases from the CABD Bioinformatics Facility for technical
767 assistance, Vladimir Benes from EMBL GeneCore for advice on sequencing of DamID libraries
768 and Delphine Larrieu for insightful comments. We also acknowledge the Caenorhabditis
769 Genetics Center (CGC), which is funded by the National Institutes of Health (NIH) Office of
770 Research Infrastructure Programs (P40 OD010440) and WormBase.

771

772 **FUNDING**

773 This project was funded by the Spanish Ministerio de Ciencia, Innovación y Universidades
774 (MCIU), Agencia Estatal de Investigación, the European Union, the European Regional

775 Development Fund (PID2019-105069GB-I00, CEX2020-001088-M, and PID2022-137162NB-I00;
776 doi:10.13039/501100011033) and the Spanish Nacional Research Council, (2023AEP058). R.R.B.
777 was supported by contract BES-2017-080216 from the Spanish MCIU and Scientific Exchange
778 Grant 9276 from EMBO. J.D.W. was supported by the National Science Foundation (NSF) Division
779 of Molecular and Cellular Biosciences (CAREER award 1942922). C.G.R. was supported by the
780 Swedish Research Council (VR) (VR2023-04383), the Swedish Cancer Society (Cancerfonden) (23
781 2994 Pj), the Novo Nordisk Foundation (NNF22OC0078353). A.K. was supported by a Karolinska
782 Institutet Doctoral Education Grant (KID).

783

784 **FIGURE LEGENDS**

785 **Figure 1. Temperature sensitive brood size and lifespan reduction caused by *baf-1(G12T)***
786 **mutation.** (A, B) Daily and total brood size was evaluated at 20°C (A) and at 25°C (B). For the
787 wild-type (WT; blue columns) control, 14 and 41 adults were analyzed at 20°C and 25°C,
788 respectively, whereas for *baf-1(G12T)* (red columns) the equivalent numbers were 11 and 42.
789 Day 0 corresponds to the 24h interval from L4 to young adult and henceforth. Unfertilized
790 oocytes (grey) were observed on *baf-1(G12T)* plates at 25°C already on day 0 and on control
791 plates from day 2. Columns and error bars represent mean and standard deviation, respectively.
792 (C, D) Presence of sperm in the spermatheca of wild-type and *baf-1(G12T)* hermaphrodites
793 grown at 25°C and expressing mCh::HIS-58 was evaluated on days 1, 2 and 3. Representative
794 images (C) with indication of spermatheca and sperm by dashed lines and arrows, respectively
795 and combined results (D) from at least 7 animals at each time point and each strain. Scale bar
796 represents 20 µM (E, F). Lifespan assay of wild-type and *baf-1(G12T)* hermaphrodites at 25°C
797 fed with either control or *daf-16* RNAi bacteria (E) or germline-ablated *glp-4(ts)* mutants
798 combined with either wild-type *baf-1* or *baf-1(G12T)* (F). Data combined from 3 (E) or 4 (F)
799 independent experiments; the number of animals is indicated in brackets. P values from two-
800 sided t-tests (A, B; asterisks and triangles refer to fertilized embryos and unfertilized oocytes,
801 respectively) and Chi-square (D-F) tests are indicated: * $p<0.05$; ** $p<0.01$; ***$p<0.001$;
802 ****$p<1e^{-9}$.

803 **Figure 2. Nuclear morphology deteriorates faster in *baf-1(G12T)* mutants.** (A-D) Morphology
804 of hypodermal nuclei was classified on day 1 and 6 of adulthood in strains expressing GFP::LMN-
805 1 (green) and mCh::HIS-58 (magenta) (A, B) or EMR-1::mCh (C, D). Confocal micrographs (A, C)
806 and combined data from 4 independent experiments (B, D) are shown. Scale bars represent 10
807 µM (A) or 5 µM (C). Classes I-IV are defined in Materials and Methods; briefly class I corresponds
808 to nuclei with smooth, regular NE morphology and classes II-IV represent increasingly irregular
809 morphologies. The number of nuclei analyzed, and statistical tests are reported in
810 Supplementary Table S1. (E, F) Quantification of GFP::LMN-1 (E) and EMR-1::mCh (F) signal in
811 the NE, nucleoplasm and cytoplasm. Data from 2 independent experiments; at least 7 animals
812 were analyzed for each strain. In these and subsequent boxplots, the midline represents the
813 median and the upper and lower limits of the box correspond to the third and first quartile,
814 respectively. The whiskers extend to the lowest and higher observations but maximum up to 1.5
815 times the interquartile range. P values from two-sided t-tests are indicated: * $p<0.05$; ** $p<0.01$.

816 **Figure 3. *baf-1(G12T)* worms are hypersensitive to GFP tagging.** (A, C) Embryonic lethality was
817 quantified for hermaphrodites carrying combinations of *baf-1(G12T)* and *gfp::lmn-1(yc32)* as
818 indicated (A) or either wild-type (+), GFP::BAF-1 (GFP) or GFP::BAF-1(G12T) (GFP::G12T) (C). Each
819 symbol represents the average per 3-5 worms. (B, D) Selected time points from confocal
820 timelapse recordings of early embryos expressing GFP::LMN-1 (green) and mCh::HIS-58
821 (magenta) (B) or either BAF-1 or BAF-1(G12T) tagged endogenously with GFP (D). Arrowheads
822 and arrows indicate abnormal (pro-)NEs and failures in chromosome segregation, respectively.
823 Time is indicated relative to P0 anaphase onset. Scale bars represent 10 µM. (E) Quantification

824 of GFP::BAF-1 (blue; n=9 adult hermaphrodites) and GFP::BAF-1(G12T) (red; n = 7) intensity at
825 the NE of hypodermal nuclei, in the nucleoplasm and in the cytoplasm. The ratio between the
826 nuclear and cytoplasmic compartment is shown in the insert. P value from two-sided t-test is
827 indicated: * p<0.05. Data from 3 independent experiments.

828 **Figure 4. Identification of tissue-specific BAF-1 and BAF-1(G12T) chromatin association.** (A)
829 Genome browser views of normalized GFP::Dam reads per 2 kb bins. The genes *mua-6* and *dod-*
830 *3*, which are expressed in hypodermis and intestine, respectively, are indicated. (B, C)
831 Normalized log2 values of Dam::BAF-1/GFP::Dam and Dam::BAF-1(G12T)/GFP::Dam ratios per
832 10 kb bins shown as genome browser view of chrII (B) and as box plots for all autosomes (C).
833 Grey bars above each track indicate enriched association to BAF-1 or BAF-1(G12T) (FDR < 0.05).
834 Chromosome arms were grouped based on the presence or absence of meiotic pairing centers
835 (PCs). P values from pairwise Wilcoxon Rank Sum Tests corrected for multiple testing (Benjamini
836 and Hochberg method): * p<0.05; ** p<0.01; ***p<0.001; ****p<$1e^{-9}$. For clarity, only selected
837 pairwise p values are indicated. (D) Normalized log2 values of Dam::BAF-1/GFP::Dam and
838 Dam::BAF-1(G12T)/GFP::Dam ratios per 2 kb bins shown as genome browser view of 500 kb
839 region from left arm of chrIII. Examples of regions enriched for association to either BAF-1 or
840 BAF-1(G12T) in the hypodermis are outlines with dashed boxed. (E, F) Venn diagram
841 representation (E) and Tissue Enrichment Analysis (F) of genes associated with BAF-1 or BAF-
842 1(G12T) in hypodermis or intestine. Total number of genes for each condition is shown in bracket
843 in E. The size and color of the circles in F reflect number of genes and p values adjusted for
844 multiple comparisons (Benjamini and Hochberg method; Q value), respectively.

845 **Figure 5. Identification of differentially expressed genes.** (A, B) Distribution of log2 values of
846 Dam::BAF-1/GFP::Dam and Dam::BAF-1(G12T)/GFP::Dam ratios per gene in hypodermis (A) and
847 intestine (B). Genes were separated in 4 categories: expressed in hypodermis and intestine (Hyp
848 & Int; 491 genes), hypodermis only (Hyp only; 1469 genes), intestine only (Int only; 1094) or not
849 detected as expressed by RAPID in any of the two tissues (Not expressed; 43330 genes). P values
850 from pairwise Wilcoxon Rank Sum Tests corrected for multiple testing (Benjamini and Hochberg
851 method) were <$2e^{-14}$ for all comparisons in the hypodermis and <$5e^{-6}$ for all comparisons in the
852 intestine. (C, D) Gene expression determined by RAPID in wild-type (x-axis) versus *baf-1(G12T)*
853 (y axis) in hypodermis (C) and intestine (D). Genes outside the dashed lines have average
854 differential log2 values >1 between the wild-type and the mutant (fold change >2). Genes
855 detected as differentially expressed in both replicas are indicated in blue (Genes up in *baf-*
856 *1(G12T)*) and red (Genes down in *baf-1(G12T)*). (E) Significant gene ontology terms identified
857 among differentially expressed genes (DEG), all combined, but also upregulated and
858 downregulated separately. The size and color of the circles reflect the number of DEGs and p
859 values adjusted for multiple comparisons (Benjamini and Hochberg method; Q value),
860 respectively.

861 **Figure 6. Differentially expressed genes bind distinctively to BAF-1 and BAF-1(G12T).** (A-B)
862 Genes with increased (A) or decreased (B) expression in intestine of *baf-1(G12T)* mutants were
863 analyzed for association to wild-type BAF-1 and BAF-1(G12T) in scatter plots (left; BAF-1
864 association on x axis; BAF-1(G12T) association on y axis) and box plots (right). Genes with
865 significantly higher association to Dam::BAF-1 or Dam::BAF-1(G12T) than to GFP::Dam are
866 indicated in red in scatter plots. Genes indicated in orange encode structural constituents of
867 ribosomes. Genes plotted in green are also deregulated in hypodermis (see **Supplementary**
868 **Figure S9**). (C) The association of differentially expressed genes encoding structural constituents
869 of ribosomes to BAF-1 and BAF-1(G12T) in intestine. P values from two-sided paired t-tests,
870 excluding outliers in A-B, are indicated.

871 **Figure 7. Altered stress resistance on *baf-1(G12T)* mutants.** (A) Survival of young adult
872 hermaphrodites as function of exposure time to 6 mM tert-Butyl hydroperoxide. Numbers in
873 brackets indicate the number of animals analysed. (B) Percentage of embryos developing into

874 larvae after exposure of young adult hermaphrodites to either 0 (left) or 25 (right) J/m^2 dose of
875 UV light. Each point represents an independent replica (n=8). (C) Survival of young adult
876 hermaphrodites as function of incubation time at 35°C. Numbers in brackets indicate the
877 number of animals analysed. P values from Chi-squared tests (A, C) and two-sided paired t-test
878 (B) are indicated.

879 **Supplementary Figure S1. *baf-1(G12T)* mutants have normal viability and lifespan at 20°C.** (A)
880 The predicted 3-dimensional structure of *C. elegans* BAF-1 (rainbow-colored; Uniprot Q03565)
881 was superimposed onto the structure of human BAF (magenta; Uniprot O75531) using iCn3D
882 Structure Viewer (Wang et al. 2022) (https://www.ncbi.nlm.nih.gov/Structure/icn3d/). Residue
883 12 is highlighted in green. (B, C) The egg laying rate (B) and embryonic viability (C) were
884 determined for hermaphrodites grown at 20°C, 25°C or shifted from 20°C to 25°C when reaching
885 adulthood. (D) Lifespan assay of wild-type and *baf-1(G12T)* hermaphrodites at 20°C. The number
886 of animals analyzed is indicated in brackets. P values from two-sided t-test (B) and Chi-square
887 test (D) are indicated: ***p<0.001.

888 **Supplementary Figure S2. Sperm defect caused by *baf-1(G12T)* mutation.** (A) Progeny
889 produced at 25°C by day 1 wild-type and *baf-1(G12T)* adults either unmated or mated with wild-
890 type or *baf-1(G12T)* males as indicated. (B, C) Total (B) and daily (C) brood size produced at 25°C
891 by feminized *fog-2* animals mated with either *fog-2* or *baf-1(G12T)* males. Error bars represent
892 standard deviation. P values from two-sided t-test are indicated: * p<0.05; ** p<0.01;
893 ***p<0.001.

894 **Supplementary Figure S3. BAF-1 and BAF-1(G12T) but not LMN-1 nor EMR-1 are present in**
895 **mature sperm.** Confocal micrographs of males (A, E) and hermaphrodites (B-D, F) expressing
896 fluorescent proteins as indicated. Animals were wild-type for *baf-1*, except *baf-1(G12T)* in C and
897 F. Spermathecae of hermaphrodites and gonads of males are outlined; arrows indicate examples
898 of sperm.

899 **Supplementary Figure S4. Nuclear morphology deteriorates faster in *baf-1(G12T)* mutants.** (A-
900 D) Morphology of hypodermal nuclei was classified on day 8 of adulthood in strains expressing
901 GFP::LMN-1 (green) and mCh::HIS-58 (magenta) (A, B) or EMR-1:.mCh (C, D). Confocal
902 micrographs (A, C) and combined data from 4 independent experiments (B, D) are shown. Scale
903 bars represent 10 µM (A) or 5 µM (C). Classes I-IV are defined in Materials and Methods; briefly,
904 class I corresponds to nuclei with smooth, regular NE morphology and classes II-IV represent
905 increasingly irregular morphologies. The number of nuclei analyzed, and statistical tests are
906 reported in Supplementary Table S1.

907 **Supplementary Figure S5. *baf-1(G12T)* worms are hypersensitive to GFP tagging of LMN-1.** (A)
908 Embryonic lethality was quantified for hermaphrodites carrying combinations of *baf-1(G12T)*
909 and *gfp::lmn-1(jf98)* as indicated. Each symbol represents the average per 3-5 worms. (B)
910 Selected time points from confocal timelapse recording of 1 control and 3 *baf-1(G12T)* embryos
911 expressing endogenously tagged GFP::LMN-1 (green; allele *yc32*) and mCh::HIS-58 (magenta).
912 Arrows indicate failures in chromosome segregation. Scale bars represent 10 µM.

913 **Supplementary Figure S6. *baf-1(G12T)* worms are hypersensitive to GFP tagging.** (A) Selected
914 time points from confocal timelapse recording of 2 GFP::BAF-1 and 2 GFP::BAF-1(G12T)
915 endogenously tagged embryos co-expressing mCh::HIS-58 (magenta). Arrows indicate failures
916 in chromosome segregation. Scale bars represent 10 µM. (B) Confocal micrographs of
917 hermaphrodites expressing endogenously tagged GFP::BAF-1 or GFP::BAF-1(G12T) as indicated.

918 **Supplementary Figure S7. Chromatin accessibility is unaffected in *baf-1(G12T)* mutants.** (A)
919 Spearman correlation values for individual GFP::Dam samples with reads binned in 2 kb regions.
920 Note that the 2 tissues (hypodermis = hyp; intestine = int) cluster separately and, within each
921 tissue, the correlations between wild-type and *baf-1(G12T)* are higher than the correlations

922 between the three replicas. (B) Genome browser views of normalized GFP::Dam reads per 2 kb
923 bins for chrII.

924 **Supplementary Figure S8. Variation in BAF-1 chromatin association is higher between tissues**
925 **than between wild-type BAF-1 and mutant BAF-1(G12T).** (A) Pearson correlation values for log2
926 values (Dam::BAF-1/GFP::Dam or Dam::BAF-1(G12T)/GFP::Dam) binned in 100 kb regions. Note
927 that the 2 tissues (hypodermis = hyp; intestine = int) cluster separately and, within each tissue,
928 the correlations between wild-type and *baf-1(G12T)* are higher than the correlations between
929 the three replicas. (B, C) Normalized log2 values of Dam::BAF-1/GFP::Dam and Dam::BAF-
930 1(G12T)/GFP::Dam ratios per 100 kb bins for the entire genome (B) and per 2 kb bins as genome
931 browser view of 500 kb region from left arm of chrI (C). For clarity, the curves in B represent
932 rolling means across 3 consecutive bins. Grey bars above each track in C indicate enriched
933 association to BAF-1 or BAF-1(G12T) (FDR < 0.05). Examples of regions enriched for association
934 to either BAF-1 or BAF-1(G12T) in the intestine are outlines with dashed boxed.

935 **Supplementary Figure S9. Differentially expressed genes encoding cuticle components bind**
936 **distinctively to BAF-1 and BAF-1(G12T).** (A-B) Genes with increased (A) or decreased (B)
937 expression in hypodermis of *baf-1(G12T)* mutants were analyzed for association to wild-type
938 BAF-1 (x axis) and BAF-1(G12T) in scatter plots (left; BAF-1 association on x axis; BAF-1(G12T)
939 association on y axis) and box plots (right). Genes with significantly higher association to
940 Dam::BAF-1 or Dam::BAF-1(G12T) than to GFP::Dam are indicated in red in scatter plots. Genes
941 indicated in orange (and *col-63* indicated in red) encode structural constituents of the cuticle.
942 Genes plotted in green are also deregulated in intestine (see **Figure 6**). (C) The association of
943 differentially expressed genes encoding structural constituents of the cuticle to BAF-1 and BAF-
944 1(G12T) in hypodermis. P values from two-sided paired t-tests, excluding outliers in A-B, are
945 indicated.

946 **Supplementary Video S1. Abnormal localization of GFP::LMN-1 and chromosome segregation**
947 **defects caused by *baf-1(G12T)*.** Control (left) and *baf-1(G12T)* (right) embryos expressing
948 GFP::LMN-1 (green) and mCh::HIS-58 (magenta) were observed by spinning disk confocal
949 microscopy every 12.5 sec. Each time point represents maximum projections of 17 confocal
950 slices. Corresponds to Figure 3B.

951 **Supplementary Video S2. Abnormal localization of GFP::BAF-1(G12T) and chromosome**
952 **segregation defects caused by *baf-1(G12T)*.** Control GFP::BAF-1 (left) and GFP::BAF-1(G12T)
953 (right) embryos co-expressing mCh::HIS-58 (magenta; GFP in green) were observed by spinning
954 disk confocal microscopy every 20.4 sec. Each time point represents maximum projections of 17
955 confocal slices. Corresponds to Figure 3D.

956

957 **REFERENCES:**

958 Ahringer J, Gasser SM. 2018. Repressive Chromatin in Caenorhabditis elegans: Establishment,
959 Composition, and Function. *Genetics* **208**: 491-511.
960 Angeles-Albores D, Lee R, Chan J, Sternberg P. 2018. Two new functions in the WormBase
961 Enrichment Suite. *MicroPubl Biol* **2018**.
962 Angeles-Albores D, RY NL, Chan J, Sternberg PW. 2016. Tissue enrichment analysis for C. elegans
963 genomics. *BMC Bioinformatics* **17**: 366.
964 Arantes-Oliveira N, Apfeld J, Dillin A, Kenyon C. 2002. Regulation of life-span by germ-line stem
965 cells in Caenorhabditis elegans. *Science* **295**: 502-505.
966 Arribere JA, Bell RT, Fu BX, Artiles KL, Hartman PS, Fire AZ. 2014. Efficient marker-free recovery
967 of custom genetic modifications with CRISPR/Cas9 in Caenorhabditis elegans. *Genetics*
968 **198**: 837-846.

969 Asencio C, Davidson IF, Santarella-Mellwig R, Ly-Hartig TB, Mall M, Wallenfang MR, Mattaj IW,
970 Gorjanacz M. 2012. Coordination of kinase and phosphatase activities by Lem4 enables
971 nuclear envelope reassembly during mitosis. *Cell* **150**: 122-135.
972 Bardou P, Mariette J, Escudie F, Djemiel C, Klopp C. 2014. jvenn: an interactive Venn diagram
973 viewer. *BMC Bioinformatics* **15**: 293.
974 Barger SR, Penfield L, Bahmanyar S. 2023. Nuclear envelope assembly relies on CHMP-7 in the
975 absence of BAF-LEM-mediated hole closure. *J Cell Sci* **136**.
976 Beanan MJ, Strome S. 1992. Characterization of a germ-line proliferation mutation in C. elegans.
977 *Development* **116**: 755-766.
978 Berman JR, Kenyon C. 2006. Germ-cell loss extends C. elegans life span through regulation of
979 DAF-16 by kri-1 and lipophilic-hormone signaling. *Cell* **124**: 1055-1068.
980 Bone CR, Chang YT, Cain NE, Murphy SP, Starr DA. 2016. Nuclei migrate through constricted
981 spaces using microtubule motors and actin networks in C. elegans hypodermal cells.
982 *Development* **143**: 4193-4202.
983 Bradley CM, Ronning DR, Ghirlando R, Craigie R, Dyda F. 2005. Structural basis for DNA bridging
984 by barrier-to-autointegration factor. *Nat Struct Mol Biol* **12**: 935-936.
985 Breusegem SY, Houghton J, Romero-Bueno R, Fragoso-Luna A, Kentistou KA, Ong KK, Janssen A,
986 Bright NA, Riedel CG, Perry JRB et al. 2022. A multiparametric anti-aging CRISPR screen
987 uncovers a role for BAF in protein translation. *bioRxiv* doi:10.1101/2022.10.07.509469.
988 Brueckner L, Zhao PA, van Schaik T, Leemans C, Sima J, Peric-Hupkes D, Gilbert DM, van Steensel
989 B. 2020. Local rewiring of genome-nuclear lamina interactions by transcription. *EMBO J*
990 **39**: e103159.
991 Cabanillas R, Cadinanos J, Villameytide JA, Perez M, Longo J, Richard JM, Alvarez R, Duran NS,
992 Illan R, Gonzalez DJ et al. 2011. Nestor-Guillermo progeria syndrome: a novel premature
993 aging condition with early onset and chronic development caused by BANF1 mutations.
994 *Am J Med Genet A* **155A**: 2617-2625.
995 Cabianca DS, Munoz-Jimenez C, Kalck V, Gaidatzis D, Padeken J, Seeber A, Askjaer P, Gasser SM.
996 2019. Active chromatin marks drive spatial sequestration of heterochromatin in C.
997 elegans nuclei. *Nature* **569**: 734-739.
998 Collins JJ, Huang C, Hughes S, Kornfeld K. 2008. The measurement and analysis of age-related
999 changes in Caenorhabditis elegans. *WormBook* doi:10.1895/wormbook.1.137.1: 1-21.
1000 Cox JL, Mallanna SK, Ormsbee BD, Desler M, Wiebe MS, Rizzino A. 2011. Banf1 is required to
1001 maintain the self-renewal of both mouse and human embryonic stem cells. *J Cell Sci* **124**:
1002 2654-2665.
1003 de la Cruz Ruiz P, Romero-Bueno R, Askjaer P. 2022. Analysis of Nuclear Pore Complexes in
1004 Caenorhabditis elegans by Live Imaging and Functional Genomics. *Methods Mol Biol*
1005 **2502**: 161-182.
1006 Dickinson DJ, Ward JD, Reiner DJ, Goldstein B. 2013. Engineering the Caenorhabditis elegans
1007 genome using Cas9-triggered homologous recombination. *Nat Methods* **10**: 1028-1034.
1008 Dobrzynska A, Askjaer P, Gruenbaum Y. 2016a. Lamin-Binding Proteins in Caenorhabditis
1009 elegans. *Methods in enzymology* **569**: 455-483.
1010 Dobrzynska A, Gonzalo S, Shanahan C, Askjaer P. 2016b. The nuclear lamina in health and
1011 disease. *Nucleus* **7**: 233-248.
1012 Donadille B, D'Anella P, Auclair M, Uhrhammer N, Sorel M, Grigorescu R, Ouzounian S, Cambonie
1013 G, Boulot P, Laforet P et al. 2013. Partial lipodystrophy with severe insulin resistance
1014 and adult progeria Werner syndrome. *Orphanet J Rare Dis* **8**: 106.
1015 Duan T, Thyagarajan S, Amoiroglou A, Rogers GC, Geyer PK. 2023. Analysis of a rare progeria
1016 variant of Barrier-to-autointegration factor in Drosophila connects centromere function
1017 to tissue homeostasis. *Cell Mol Life Sci* **80**: 73.
1018 Fisher HG, Patni N, Scheuerle AE. 2020. An additional case of Nestor-Guillermo progeria
1019 syndrome diagnosed in early childhood. *Am J Med Genet A* **182**: 2399-2402.

1020 Fragoso-Luna A, Askjaer P. 2023. The Nuclear Envelope in Ageing and Progeria. *Subcell Biochem*
1021 **102**: 53-75.
1022 Fragoso-Luna A, Romero-Bueno R, Eibl M, Ayuso C, Munoz-Jimenez C, Benes V, Cases I, Askjaer
1023 P. 2023. Expanded FLP toolbox for spatiotemporal protein degradation and
1024 transcriptomic profiling in Caenorhabditis elegans. *Genetics* **223**.
1025 Friedland AE, Tzur YB, Esvelt KM, Colaiacovo MP, Church GM, Calarco JA. 2013. Heritable
1026 genome editing in C. elegans via a CRISPR-Cas9 system. *Nat Methods* **10**: 741-743.
1027 Frøkjær-Jensen C, Davis MW, Ailion M, Jorgensen EM. 2012. Improved Mos1-mediated
1028 transgenesis in C. elegans. *Nat Methods* **9**: 117-118.
1029 Frøkjær-Jensen C, Davis MW, Hopkins CE, Newman BJ, Thummel JM, Olesen SP, Grunnet M,
1030 Jorgensen EM. 2008. Single-copy insertion of transgenes in Caenorhabditis elegans. *Nat*
1031 *Genet* **40**: 1375-1383.
1032 Furukawa K, Sugiyama S, Osouda S, Goto H, Inagaki M, Horigome T, Omata S, McConnell M,
1033 Fisher PA, Nishida Y. 2003. Barrier-to-autointegration factor plays crucial roles in cell
1034 cycle progression and nuclear organization in Drosophila. *J Cell Sci* **116**: 3811-3823.
1035 Gerstein MB Lu ZJ Van Nostrand EL Cheng C Arshinoff BI Liu T Yip KY Robilotto R Rechtsteiner A
1036 Ikegami K et al. 2010. Integrative analysis of the Caenorhabditis elegans genome by the
1037 modENCODE project. *Science* **330**: 1775-1787.
1038 Gomez-Saldivar G, Osuna-Luque J, Semple JI, Glauser DA, Jarriault S, Meister P. 2020. Tissue-
1039 Specific Transcription Footprinting Using RNA PoI DamID (RAPID) in Caenorhabditis
1040 elegans. *Genetics* doi:10.1534/genetics.120.303774.
1041 Gonzalez-Aguilera C, Ikegami K, Ayuso C, de Luis A, Iniguez M, Cabello J, Lieb JD, Askjaer P. 2014.
1042 Genome-wide analysis links emerin to neuromuscular junction activity in Caenorhabditis
1043 elegans. *Genome Biol* **15**: R21.
1044 Gonzalo S, Kreienkamp R, Askjaer P. 2017. Hutchinson-Gilford Progeria Syndrome: A premature
1045 aging disease caused by LMNA gene mutations. *Ageing Res Rev* **33**: 18-29.
1046 Gorjanacz M, Klerkx EP, Galy V, Santarella R, Lopez-Iglesias C, Askjaer P, Mattaj IW. 2007.
1047 Caenorhabditis elegans BAF-1 and its kinase VRK-1 participate directly in post-mitotic
1048 nuclear envelope assembly. *EMBO J* **26**: 132-143.
1049 Haithcock E, Dayani Y, Neufeld E, Zahand AJ, Feinstein N, Mattout A, Gruenbaum Y, Liu J. 2005.
1050 Age-related changes of nuclear architecture in Caenorhabditis elegans. *Proc Natl Acad*
1051 *Sci U S A* **102**: 16690-16695.
1052 Halfmann CT, Sears RM, Katiyar A, Busselman BW, Aman LK, Zhang Q, O'Bryan CS, Angelini TE,
1053 Lele TP, Roux KJ. 2019. Repair of nuclear ruptures requires barrier-to-autointegration
1054 factor. *J Cell Biol* **218**: 2136-2149.
1055 Haraguchi T, Kojidani T, Koujin T, Shimi T, Osakada H, Mori C, Yamamoto A, Hiraoka Y. 2008. Live
1056 cell imaging and electron microscopy reveal dynamic processes of BAF-directed nuclear
1057 envelope assembly. *J Cell Sci* **121**: 2540-2554.
1058 Haraguchi T, Koujin T, Segura-Totten M, Lee KK, Matsuoka Y, Yoneda Y, Wilson KL, Hiraoka Y.
1059 2001. BAF is required for emerin assembly into the reforming nuclear envelope. *J Cell*
1060 *Sci* **114**: 4575-4585.
1061 Hsin H, Kenyon C. 1999. Signals from the reproductive system regulate the lifespan of C. elegans.
1062 *Nature* **399**: 362-366.
1063 Ikegami K, Egelhofer TA, Strome S, Lieb JD. 2010. Caenorhabditis elegans chromosome arms are
1064 anchored to the nuclear membrane via discontinuous association with LEM-2. *Genome*
1065 *Biol* **11**: R120.
1066 Janssen A, Marcelot A, Breusegem S, Legrand P, Zinn-Justin S, Larrieu D. 2022. The BAF A12T
1067 mutation disrupts lamin A/C interaction, impairing robust repair of nuclear envelope
1068 ruptures in Nestor-Guillermo progeria syndrome cells. *Nucleic Acids Res*
1069 doi:10.1093/nar/gkac726.

1070 Kamath RS, Fraser AG, Dong Y, Poulin G, Durbin R, Gotta M, Kanapin A, Le Bot N, Moreno S,
1071 Sohrmann M et al. 2003. Systematic functional analysis of the Caenorhabditis elegans
1072 genome using RNAi. *Nature* **421**: 231-237.
1073 Katsanos D, Ferrando-Marco M, Razzaq I, Aughey G, Southall TD, Barkoulas M. 2021. Gene
1074 expression profiling of epidermal cell types in C. elegans using Targeted DamID.
1075 *Development* **148**.
1076 Kent WJ, Sugnet CW, Furey TS, Roskin KM, Pringle TH, Zahler AM, Haussler D. 2002. The human
1077 genome browser at UCSC. *Genome Res* **12**: 996-1006.
1078 Kind J, van Steensel B. 2014. Stochastic genome-nuclear lamina interactions: modulating roles
1079 of Lamin A and BAF. *Nucleus* **5**: 124-130.
1080 Kono Y, Adam SA, Sato Y, Reddy KL, Zheng Y, Medalia O, Goldman RD, Kimura H, Shimi T. 2022.
1081 Nucleoplasmic lamin C rapidly accumulates at sites of nuclear envelope rupture with
1082 BAF and cGAS. *J Cell Biol* **221**.
1083 Kubben N, Zhang W, Wang L, Voss TC, Yang J, Qu J, Liu GH, Misteli T. 2016. Repression of the
1084 Antioxidant NRF2 Pathway in Premature Aging. *Cell* **165**: 1361-1374.
1085 Lee MS, Craigie R. 1998. A previously unidentified host protein protects retroviral DNA from
1086 autointegration. *Proc Natl Acad Sci U S A* **95**: 1528-1533.
1087 Lin Q, Yu B, Wang X, Zhu S, Zhao G, Jia M, Huang F, Xu N, Ren H, Jiang Q et al. 2020. K6-linked
1088 SUMOylation of BAF regulates nuclear integrity and DNA replication in mammalian cells.
1089 *Proc Natl Acad Sci U S A* **117**: 10378-10387.
1090 Link J, Jantsch V. 2019. Meiotic chromosomes in motion: a perspective from Mus musculus and
1091 Caenorhabditis elegans. *Chromosoma* **128**: 317-330.
1092 Love MI, Huber W, Anders S. 2014. Moderated estimation of fold change and dispersion for RNA-
1093 seq data with DESeq2. *Genome Biol* **15**: 550.
1094 Manzo SG, Dauban L, van Steensel B. 2022. Lamina-associated domains: Tethers and looseners.
1095 *Curr Opin Cell Biol* **74**: 80-87.
1096 Marcelot A, Petitalot A, Ropars V, Le Du MH, Samson C, Dubois S, Hoffmann G, Miron S, Cuniasse
1097 P, Marquez JA et al. 2021. Di-phosphorylated BAF shows altered structural dynamics and
1098 binding to DNA, but interacts with its nuclear envelope partners. *Nucleic Acids Res* **49**:
1099 3841-3855.
1100 Margalit A, Neufeld E, Feinstein N, Wilson KL, Podbilewicz B, Gruenbaum Y. 2007. Barrier to
1101 autointegration factor blocks premature cell fusion and maintains adult muscle integrity
1102 in C. elegans. *J Cell Biol* **178**: 661-673.
1103 Margalit A, Segura-Totten M, Gruenbaum Y, Wilson KL. 2005. Barrier-to-autointegration factor
1104 is required to segregate and enclose chromosomes within the nuclear envelope and
1105 assemble the nuclear lamina. *Proc Natl Acad Sci U S A* **102**: 3290-3295.
1106 Marshall OJ, Brand AH. 2015. damidseq_pipeline: an automated pipeline for processing DamID
1107 sequencing datasets. *Bioinformatics* **31**: 3371-3373.
1108 Molitor TP, Traktman P. 2014. Depletion of the protein kinase VRK1 disrupts nuclear envelope
1109 morphology and leads to BAF retention on mitotic chromosomes. *Mol Biol Cell* **25**: 891-
1110 903.
1111 Morales-Martinez A, Dobrzynska A, Askjaer P. 2015. Inner nuclear membrane protein LEM-2 is
1112 required for correct nuclear separation and morphology in C. elegans. *J Cell Sci* **128**:
1113 1090-1096.
1114 Munoz-Jimenez C, Ayuso C, Dobrzynska A, Torres-Mendez A, Ruiz PC, Askjaer P. 2017. An
1115 Efficient FLP-Based Toolkit for Spatiotemporal Control of Gene Expression in
1116 Caenorhabditis elegans. *Genetics* **206**: 1763-1778.
1117 Nichols RJ, Wiebe MS, Traktman P. 2006. The Vaccinia-related Kinases Phosphorylate the N'
1118 Terminus of BAF, Regulating Its Interaction with DNA and Its Retention in the Nucleus.
1119 *Mol Biol Cell* **17**: 2451-2464.

1120 Paix A, Folkmann A, Rasoloson D, Seydoux G. 2015. High Efficiency, Homology-Directed Genome
1121 Editing in Caenorhabditis elegans Using CRISPR-Cas9 Ribonucleoprotein Complexes.
1122 *Genetics* **201**: 47-54.
1123 Paquet N, Box JK, Ashton NW, Suraweera A, Croft LV, Urquhart AJ, Bolderson E, Zhang SD,
1124 O'Byrne KJ, Richard DJ. 2014. Nestor-Guillermo Progeria Syndrome: a biochemical
1125 insight into Barrier-to-Autointegration Factor 1, alanine 12 threonine mutation. *BMC*
1126 *Mol Biol* **15**: 27.
1127 Perez-Jimenez MM, Rodriguez-Palero MJ, Rodenas E, Askjaer P, Munoz MJ. 2014. Age-
1128 dependent changes of nuclear morphology are uncoupled from longevity in
1129 Caenorhabditis elegans IGF/insulin receptor daf-2 mutants. *Biogerontology* **15**: 279-288.
1130 Puente XS, Quesada V, Osorio FG, Cabanillas R, Cadinanos J, Fraile JM, Ordonez GR, Puente DA,
1131 Gutierrez-Fernandez A, Fanjul-Fernandez M et al. 2011. Exome sequencing and
1132 functional analysis identifies BANF1 mutation as the cause of a hereditary progeroid
1133 syndrome. *American journal of human genetics* **88**: 650-656.
1134 Rodenas E, Gonzalez-Aguilera C, Ayuso C, Askjaer P. 2012. Dissection of the NUP107 nuclear
1135 pore subcomplex reveals a novel interaction with spindle assembly checkpoint protein
1136 MAD1 in Caenorhabditis elegans. *Mol Biol Cell* **23**: 930-944.
1137 Samson C, Petitalot A, Celli F, Herrada I, Ropars V, Le Du MH, Nhiri N, Jacquet E, Arteni AA,
1138 Buendia B et al. 2018. Structural analysis of the ternary complex between lamin A/C,
1139 BAF and emerin identifies an interface disrupted in autosomal recessive progeroid
1140 diseases. *Nucleic Acids Res* doi:10.1093/nar/gky736.
1141 Samwer M, Schneider MWG, Hoefler R, Schmalhorst PS, Jude JG, Zuber J, Gerlich DW. 2017. DNA
1142 Cross-Bridging Shapes a Single Nucleus from a Set of Mitotic Chromosomes. *Cell* **170**:
1143 956-972 e923.
1144 Schindelin J, Arganda-Carreras I, Frise E, Kaynig V, Longair M, Pietzsch T, Preibisch S, Rueden C,
1145 Saalfeld S, Schmid B et al. 2012. Fiji: an open-source platform for biological-image
1146 analysis. *Nat Methods* **9**: 676-682.
1147 Schwartz ML, Jorgensen EM. 2016. SapTrap, a Toolkit for High-Throughput CRISPR/Cas9 Gene
1148 Modification in Caenorhabditis elegans. *Genetics* **202**: 1277-1288.
1149 Sears RM, Roux KJ. 2020. Diverse cellular functions of barrier-to-autointegration factor and its
1150 roles in disease. *J Cell Sci* **133**.
1151 Sharma R, Ritler D, Meister P. 2016. Tools for DNA adenine methyltransferase identification
1152 analysis of nuclear organization during C. elegans development. *Genesis* **54**: 151-159.
1153 Shin JY, Worman HJ. 2022. Molecular Pathology of Laminopathies. *Annu Rev Pathol* **17**: 159-180.
1154 Soo SK, Rudich ZD, Ko B, Moldakozhayev A, AlOkda A, Van Raamsdonk JM. 2023. Biological
1155 resilience and aging: Activation of stress response pathways contributes to lifespan
1156 extension. *Ageing Res Rev* **88**: 101941.
1157 Southall TD, Gold KS, Egger B, Davidson CM, Caygill EE, Marshall OJ, Brand AH. 2013. Cell-type-
1158 specific profiling of gene expression and chromatin binding without cell isolation:
1159 assaying RNA Pol II occupancy in neural stem cells. *Dev Cell* **26**: 101-112.
1160 Stiernagle T. 2006. Maintenance of C. elegans. *WormBook* doi:10.1895/wormbook.1.101.1: 1-
1161 11.
1162 Stroustrup N, Ulmschneider BE, Nash ZM, Lopez-Moyado IF, Apfeld J, Fontana W. 2013. The
1163 Caenorhabditis elegans Lifespan Machine. *Nat Methods* **10**: 665-670.
1164 Team R. 2020. RStudio: Integrated Development Environment for R. pp. RStudio, PBC.
1165 Towbin BD, Gonzalez-Aguilera C, Sack R, Gaidatzis D, Kalck V, Meister P, Askjaer P, Gasser SM.
1166 2012. Step-Wise Methylation of Histone H3K9 Positions Heterochromatin at the Nuclear
1167 Periphery. *Cell* **150**: 934-947.
1168 Turgay Y, Eibauer M, Goldman AE, Shimi T, Khayat M, Ben-Harush K, Dubrovsky-Gaupp A, Sapra
1169 KT, Goldman RD, Medalia O. 2017. The molecular architecture of lamins in somatic cells.
1170 *Nature* **543**: 261-264.

1171 Ungricht R, Kutay U. 2017. Mechanisms and functions of nuclear envelope remodelling. *Nat Rev*
1172 *Mol Cell Biol* doi:10.1038/nrm.2016.153.
1173 Unnikannan CP, Reuveny A, Grunberg D, Volk T. 2020. Recruitment of BAF to the nuclear
1174 envelope couples the LINC complex to endoreplication. *Development* **147**.
1175 Wang J, Youkharibache P, Marchler-Bauer A, Lanczycki C, Zhang D, Lu S, Madej T, Marchler GH,
1176 Cheng T, Chong LC et al. 2022. iCn3D: From Web-Based 3D Viewer to Structural Analysis
1177 Tool in Batch Mode. *Front Mol Biosci* **9**: 831740.
1178 Wang S, Stoops E, Cp U, Markus B, Reuveny A, Ordan E, Volk T. 2018. Mechanotransduction via
1179 the LINC complex regulates DNA replication in myonuclei. *J Cell Biol* **217**: 2005-2018.
1180 Ward JD. 2015. Rapid and Precise Engineering of the Caenorhabditis elegans Genome with
1181 Lethal Mutation Co-Conversion and Inactivation of NHEJ Repair. *Genetics* **199**: 363-377.
1182 Wolf N, Hirsh D, McIntosh JR. 1978. Spermatogenesis in males of the free-living nematode,
1183 Caenorhabditis elegans. *J Ultrastruct Res* **63**: 155-169.
1184 Yamamoto S, Kanca O, Wangler MF, Bellen HJ. 2024. Integrating non-mammalian model
1185 organisms in the diagnosis of rare genetic diseases in humans. *Nat Rev Genet* **25**: 46-60.
1186 Young AM, Gunn AL, Hatch EM. 2020. BAF facilitates interphase nuclear membrane repair
1187 through recruitment of nuclear transmembrane proteins. *Mol Biol Cell* **31**: 1551-1560.
1188 Zheng R, Ghirlando R, Lee MS, Mizuuchi K, Krause M, Craigie R. 2000. Barrier-to-autointegration
1189 factor (BAF) bridges DNA in a discrete, higher-order nucleoprotein complex. *Proc Natl*
1190 *Acad Sci U S A* **97**: 8997-9002.
1191

Figure 1

A

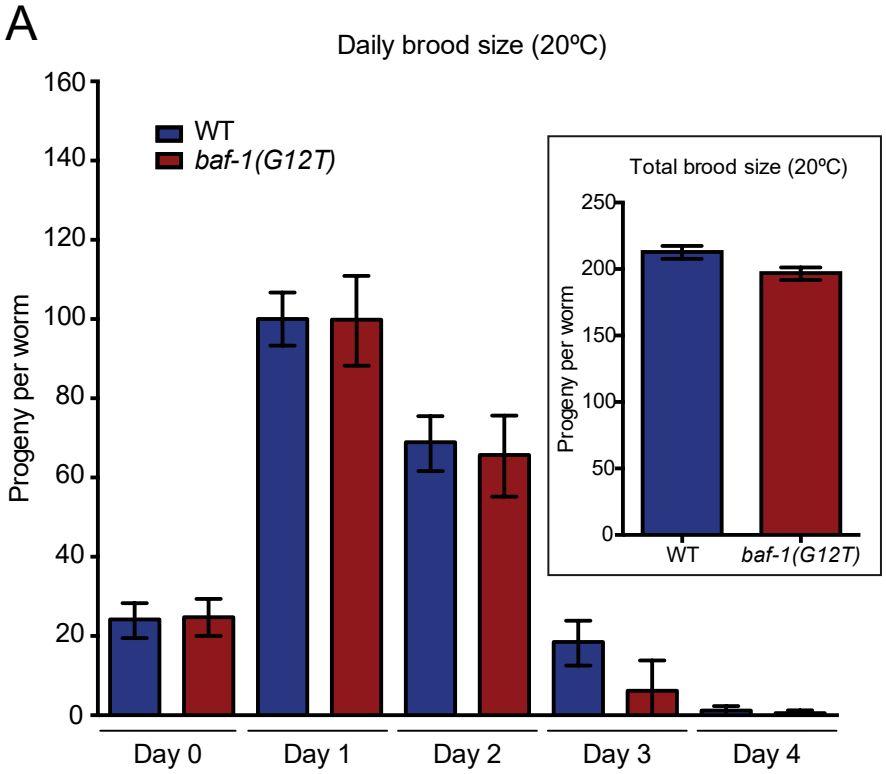

B

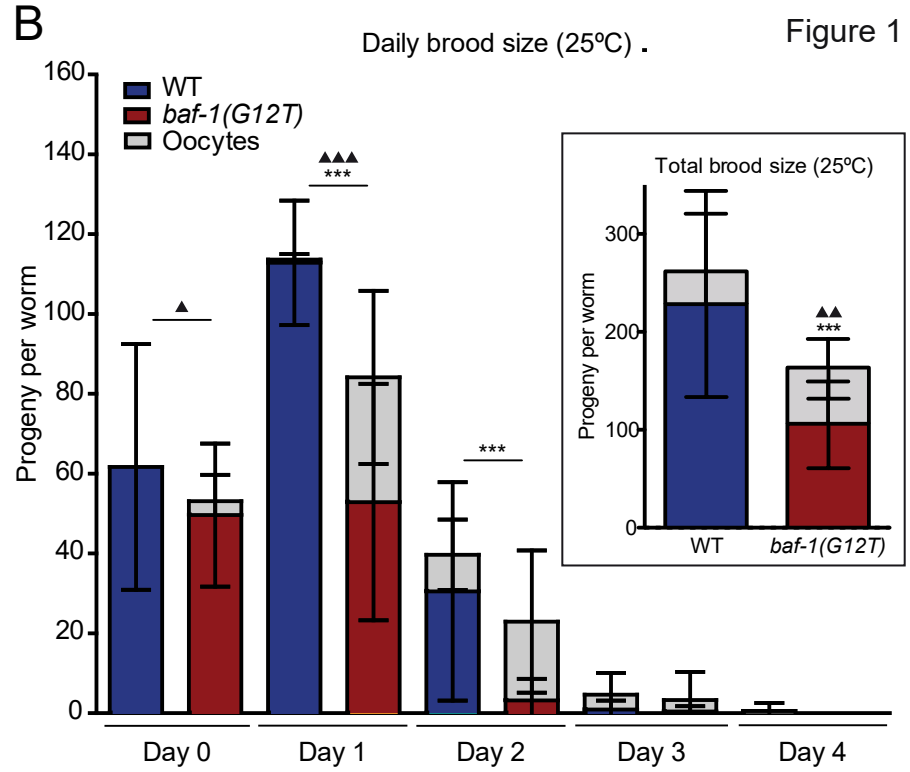

C

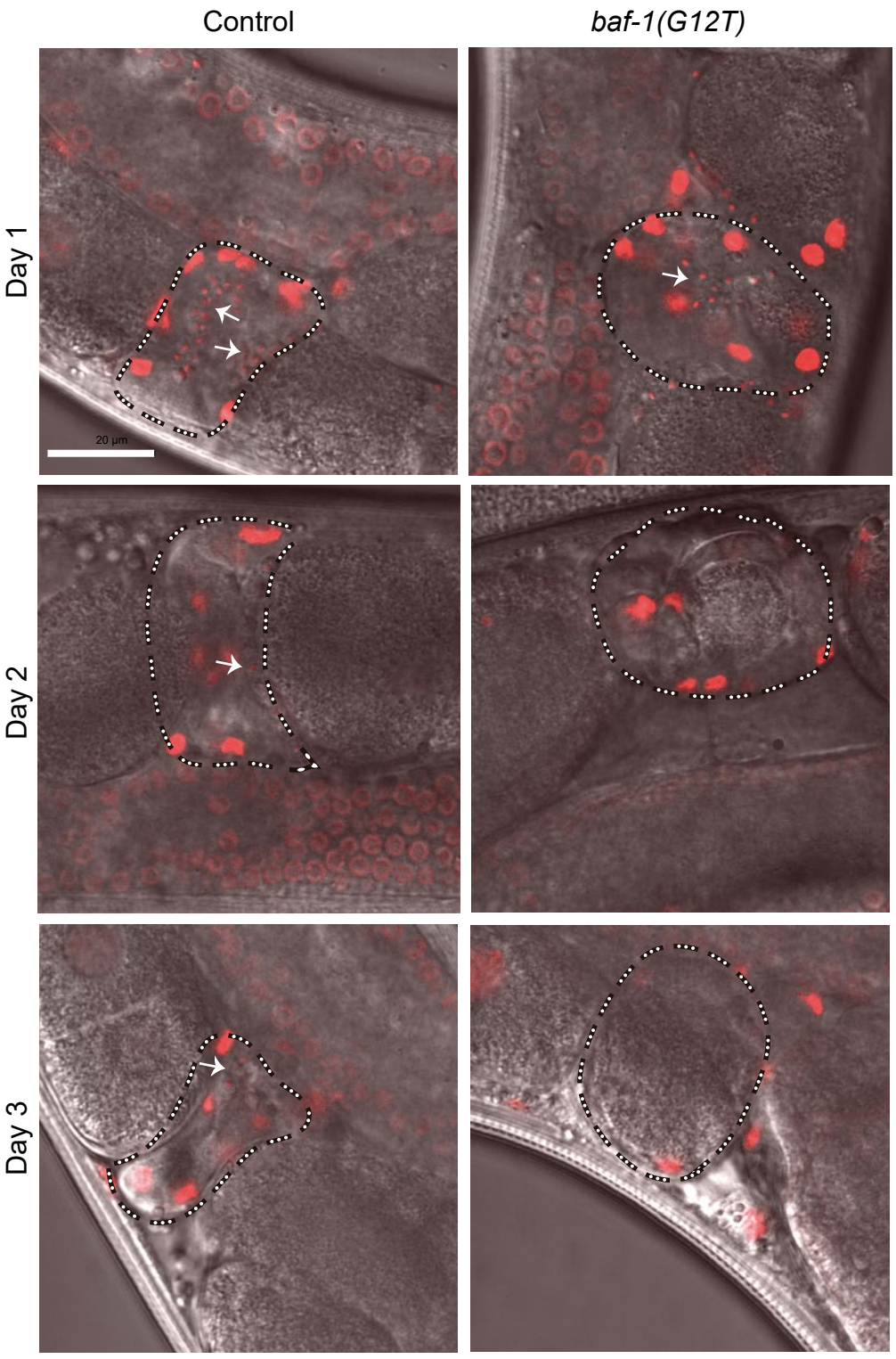

D

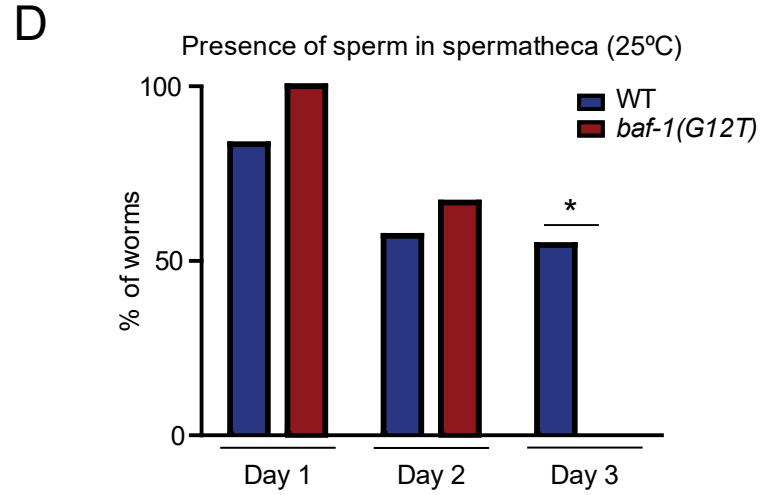

E

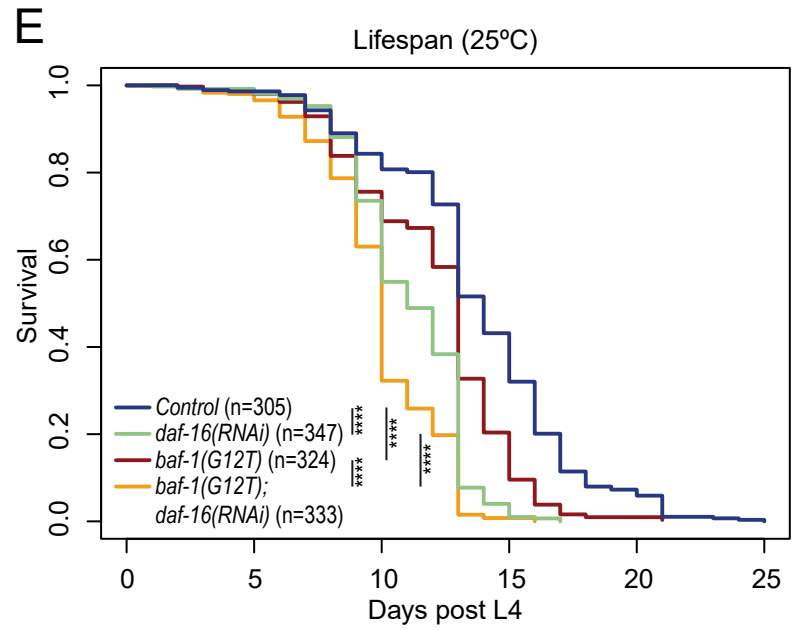

F

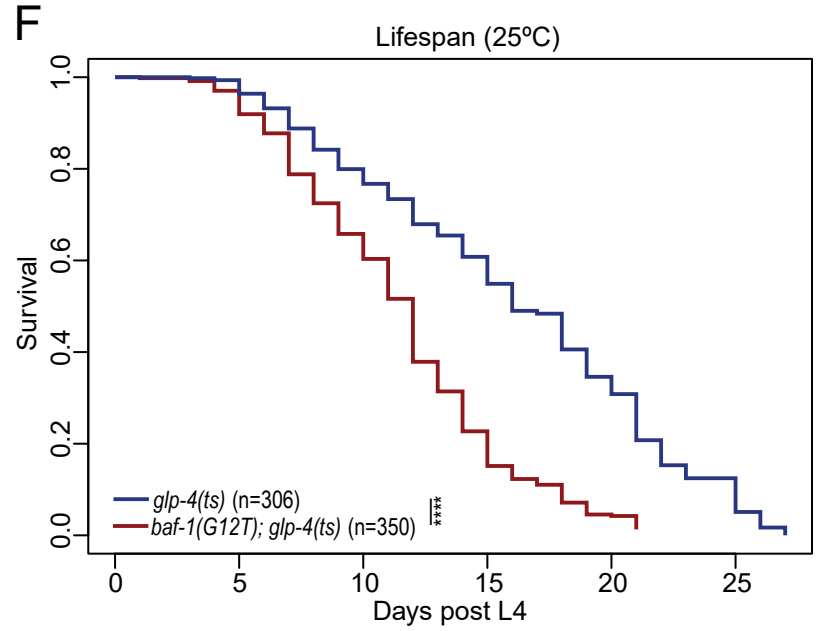

Figure 2

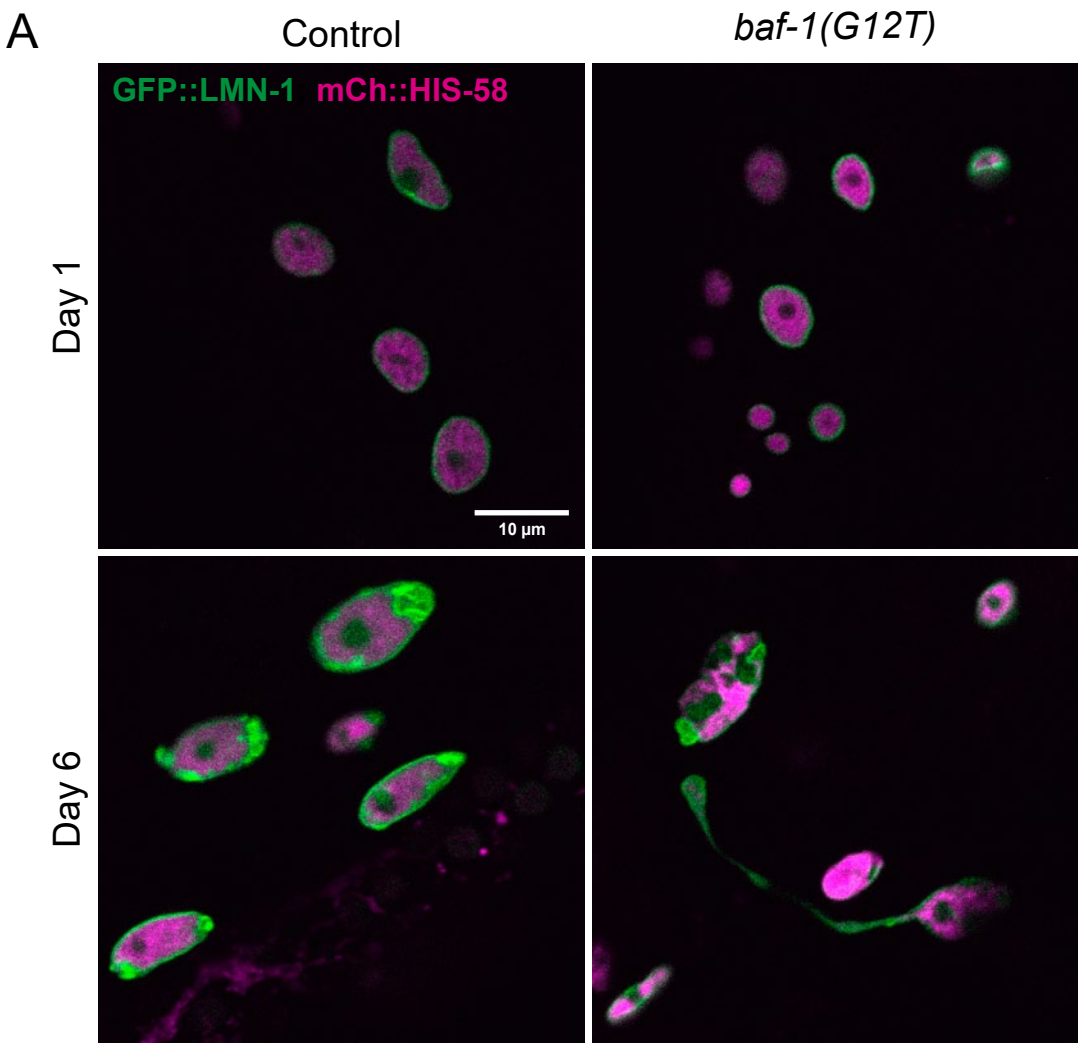
A
Control
baf-1(G12T)
GFP::LMN-1 mCh::HIS-58
Day 1
Day 6
10 µm

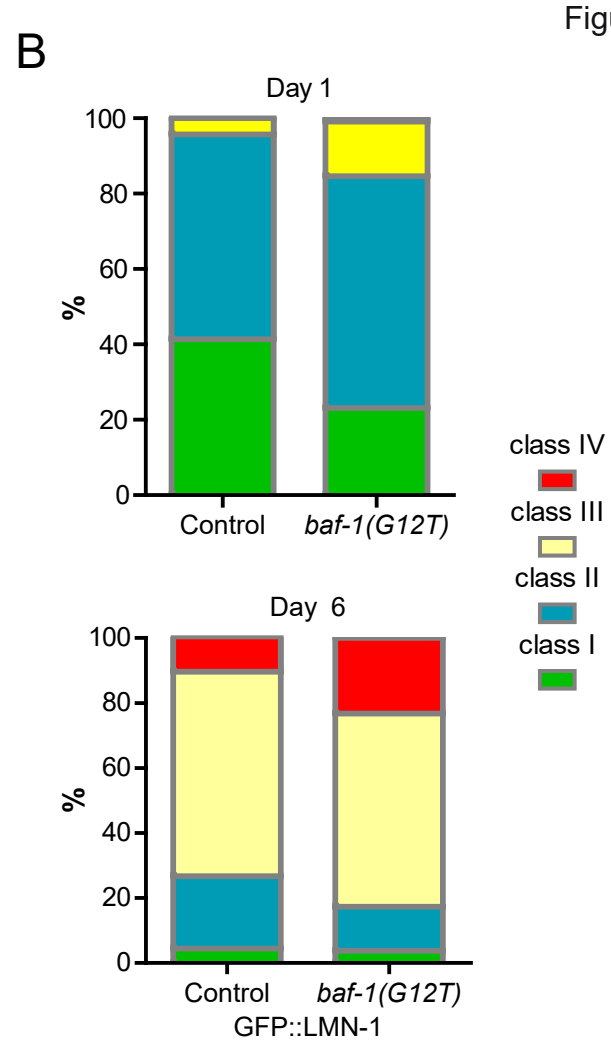
B
Day 1
Day 6
%
100
80
60
40
20
0
Control
baf-1(G12T)
GFP::LMN-1
class IV
class III
class II
class I

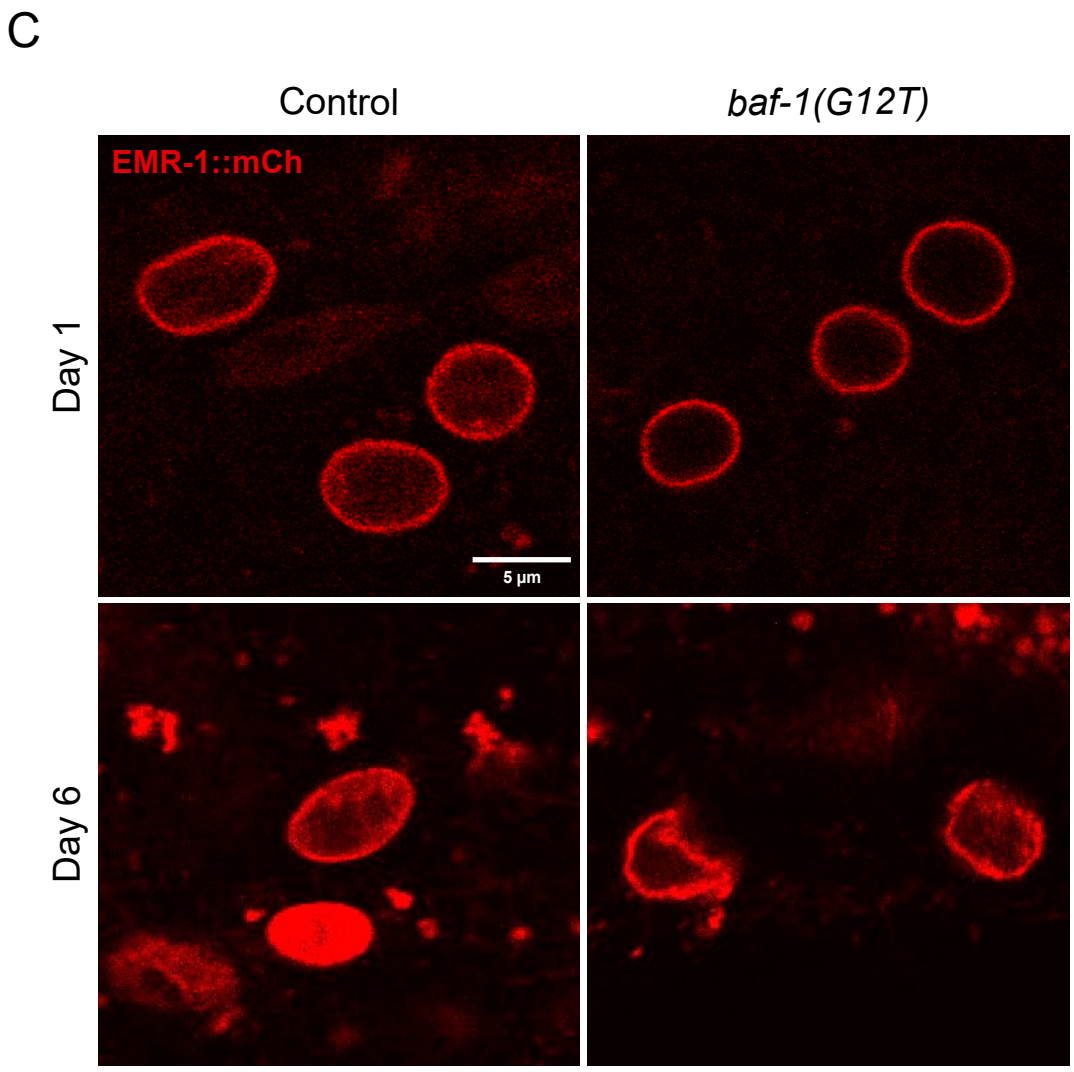
C
Control
baf-1(G12T)
EMR-1::mCh
Day 1
Day 6
5 µm

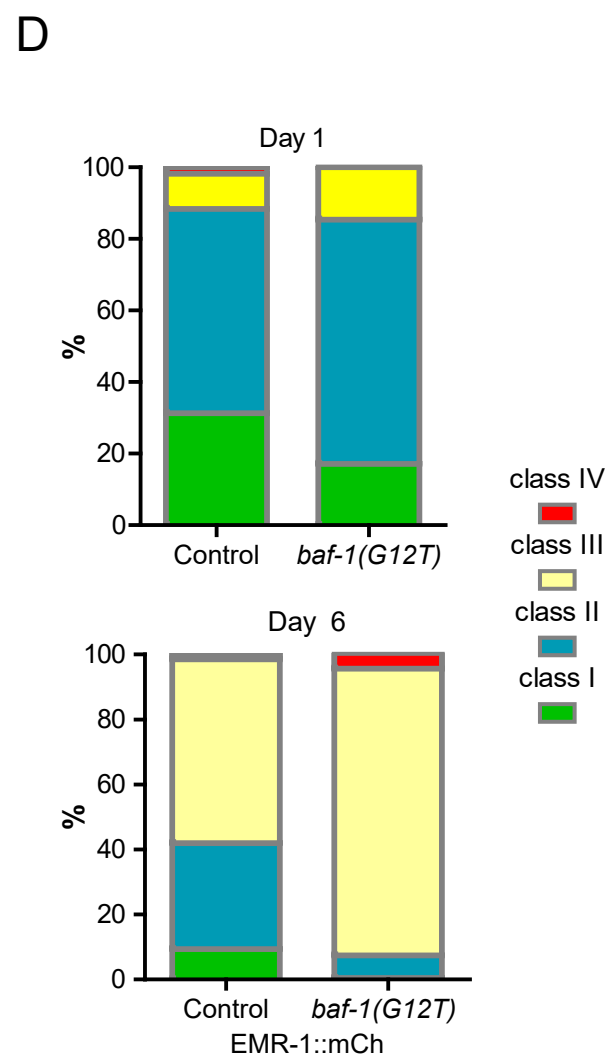
D
Day 1
Day 6
%
100
80
60
40
20
0
Control
baf-1(G12T)
EMR-1::mCh
class IV
class III
class II
class I

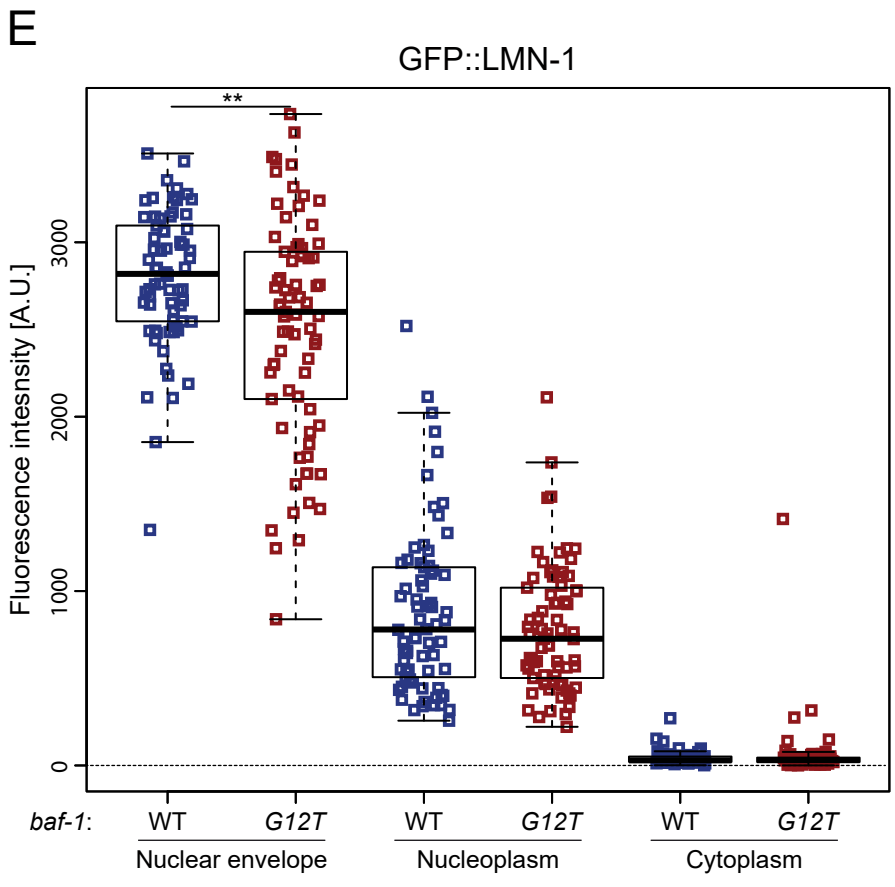
E
GFP::LMN-1
Fluorescence intesnsity [A.U.]
0
1000
2000
3000
**
baf-1:
WT
G12T
WT
G12T
WT
G12T
Nuclear envelope
Nucleoplasm
Cytoplasm

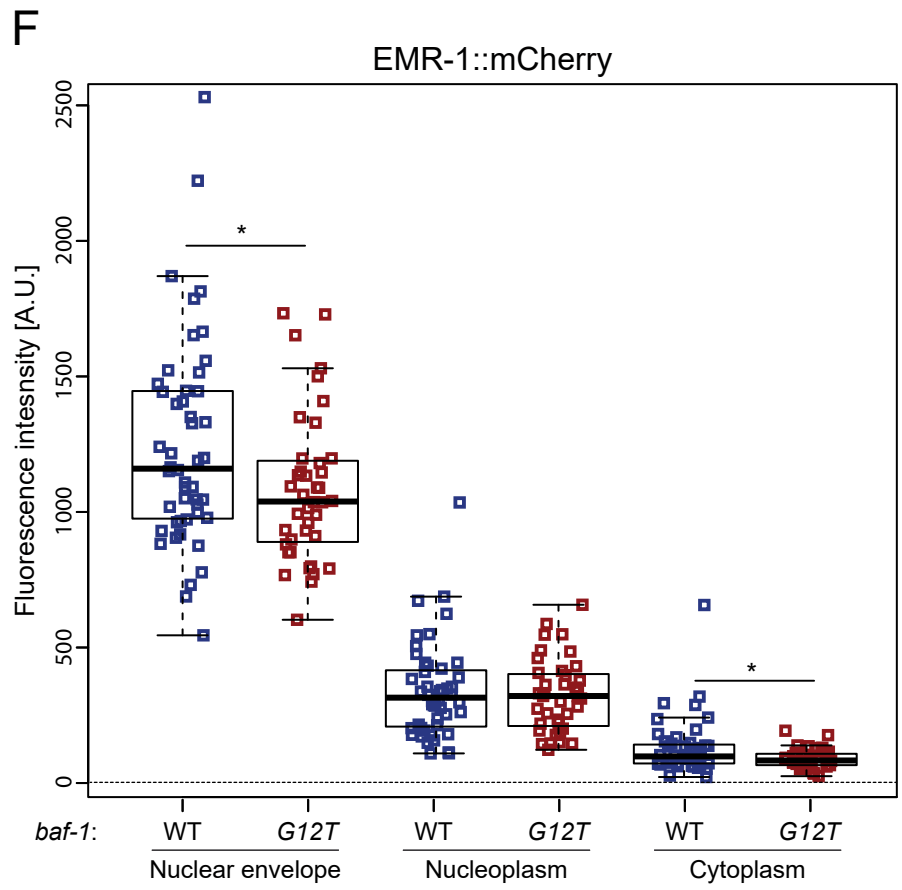
F
EMR-1::mCherry
Fluorescence intesnsity [A.U.]
0
500
1000
1500
2000
2500
*
*
baf-1:
WT
G12T
WT
G12T
WT
G12T
Nuclear envelope
Nucleoplasm
Cytoplasm

Figure 3

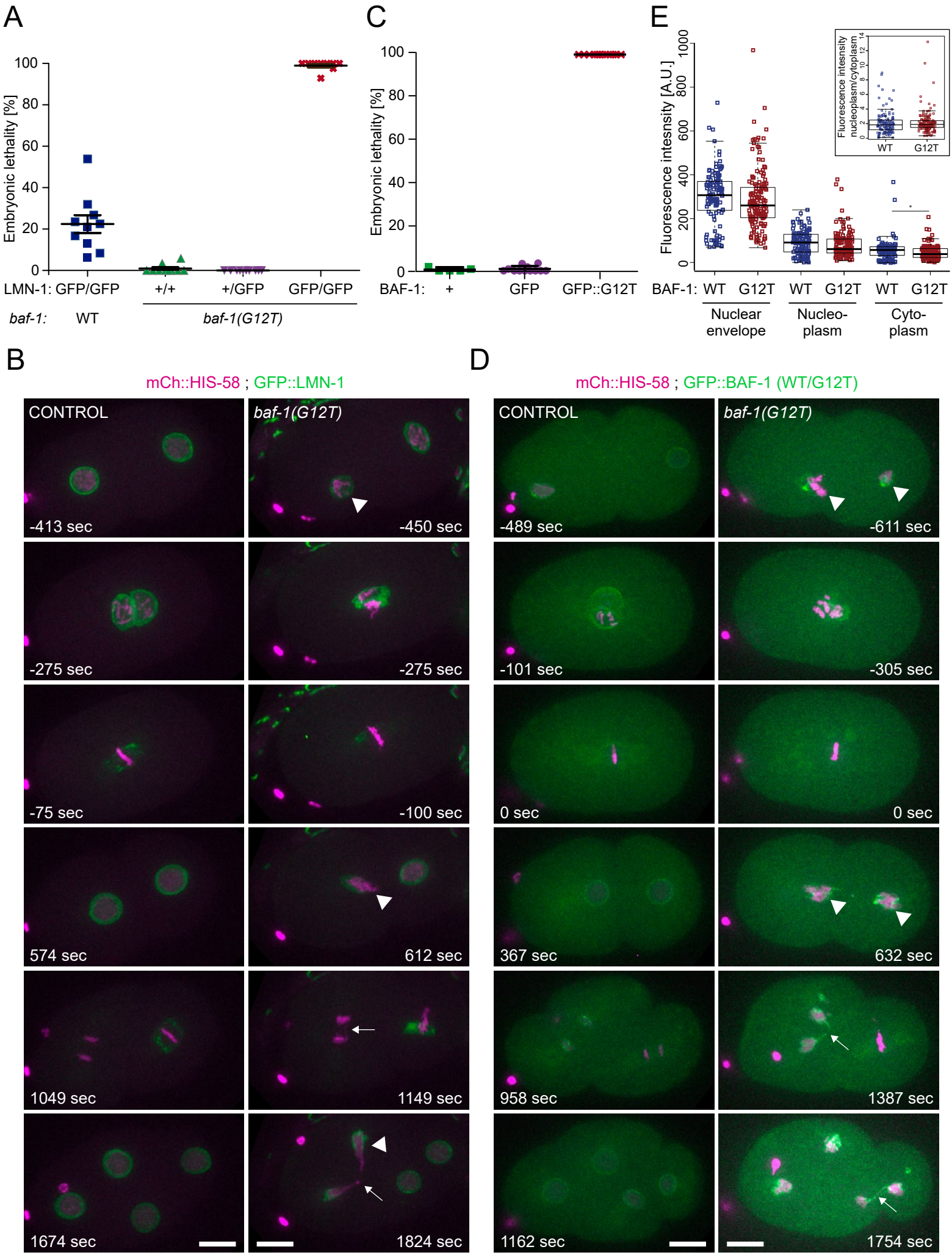
A
Embryonic lethality [%]
100
80
60
40
20
0
LMN-1: GFP/GFP
+/+
+/GFP
GFP/GFP
baf-1:
WT
baf-1(G12T)
C
Embryonic lethality [%]
BAF-1:
+
GFP
GFP::G12T
E
Fluorescence intesnsity [A.U.]
1000
800
600
400
200
0
Fluorescence intesnsity nucleoplasm/cytoplasm
WT
G12T
BAF-1: WT G12T WT G12T WT G12T
Nuclear envelope
Nucleo-plasm
Cyto-plasm
B
mCh::HIS-58 ; GFP::LMN-1
CONTROL
baf-1(G12T)
-413 sec
-450 sec
-275 sec
-275 sec
-75 sec
-100 sec
574 sec
612 sec
1049 sec
1149 sec
1674 sec
1824 sec
D
mCh::HIS-58 ; GFP::BAF-1 (WT/G12T)
CONTROL
baf-1(G12T)
-489 sec
-611 sec
-101 sec
-305 sec
0 sec
0 sec
367 sec
632 sec
958 sec
1387 sec
1162 sec
1754 sec

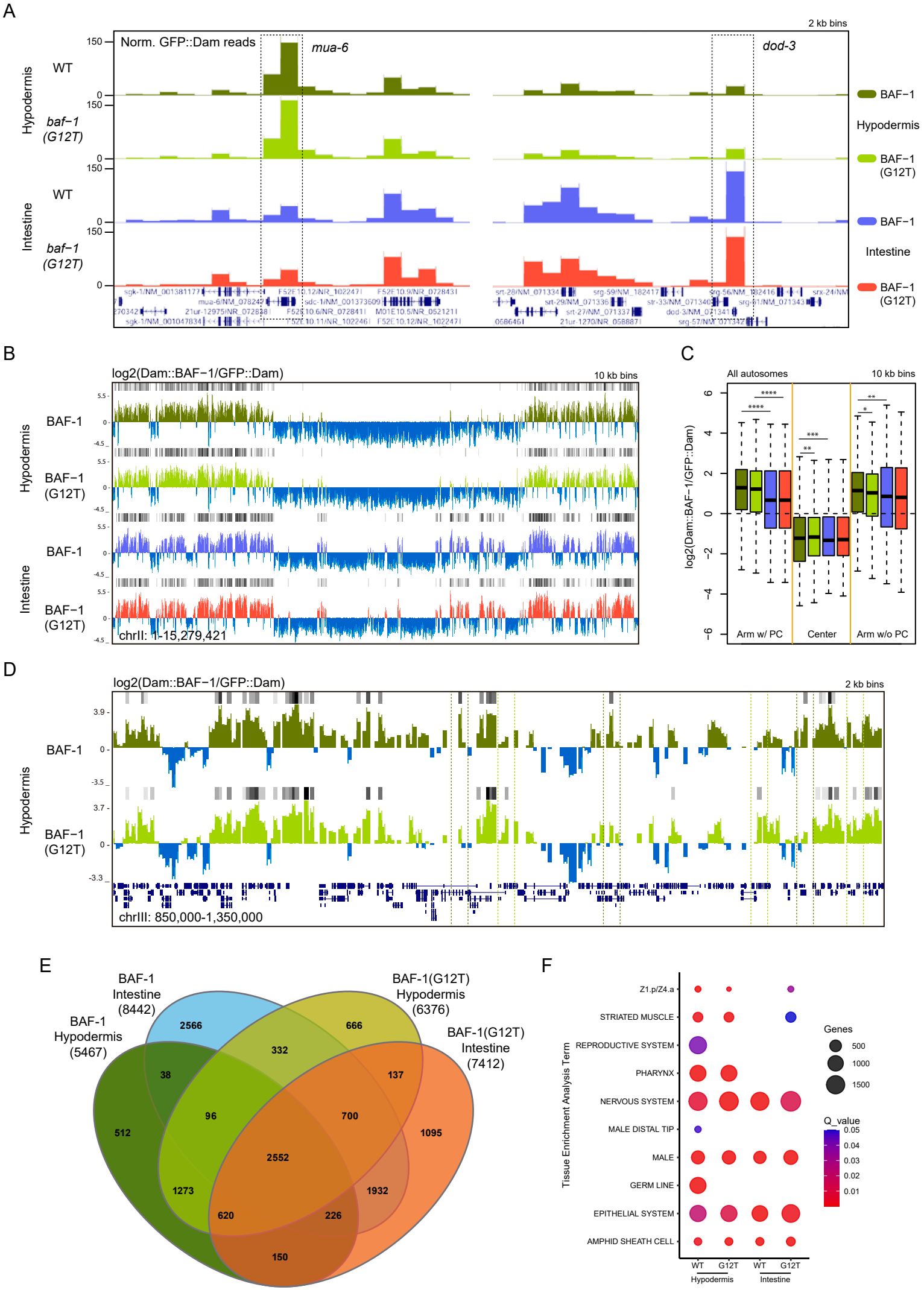
A
Norm. GFP::Dam reads
mua-6
dod-3
2 kb bins
Hypodermis
WT
baf−1 (G12T)
Intestine
WT
baf−1 (G12T)
BAF−1
Hypodermis
BAF−1 (G12T)
BAF−1
Intestine
BAF−1 (G12T)
B
log2(Dam::BAF−1/GFP::Dam)
10 kb bins
Hypodermis
BAF-1
BAF−1 (G12T)
Intestine
BAF-1
BAF−1 (G12T)
chrII: 1-15,279,421
C
All autosomes
10 kb bins
log2(Dam::BAF−1/GFP::Dam)
Arm w/ PC
Center
Arm w/o PC
D
log2(Dam::BAF−1/GFP::Dam)
2 kb bins
Hypodermis
BAF-1
BAF−1 (G12T)
chrIII: 850,000-1,350,000
E
BAF-1 Intestine (8442)
BAF-1(G12T) Hypodermis (6376)
BAF-1 Hypodermis (5467)
BAF-1(G12T) Intestine (7412)
2566
666
332
38
137
96
700
512
1095
2552
1273
1932
620
226
150
F
Tissue Enrichment Analysis Term
Z1.p/Z4.a
STRIATED MUSCLE
REPRODUCTIVE SYSTEM
PHARYNX
NERVOUS SYSTEM
MALE DISTAL TIP
MALE
GERM LINE
EPITHELIAL SYSTEM
AMPHID SHEATH CELL
WT
G12T
WT
G12T
Hypodermis
Intestine
Genes
500
1000
1500
Q_value
0.05
0.04
0.03
0.02
0.01

Figure 5

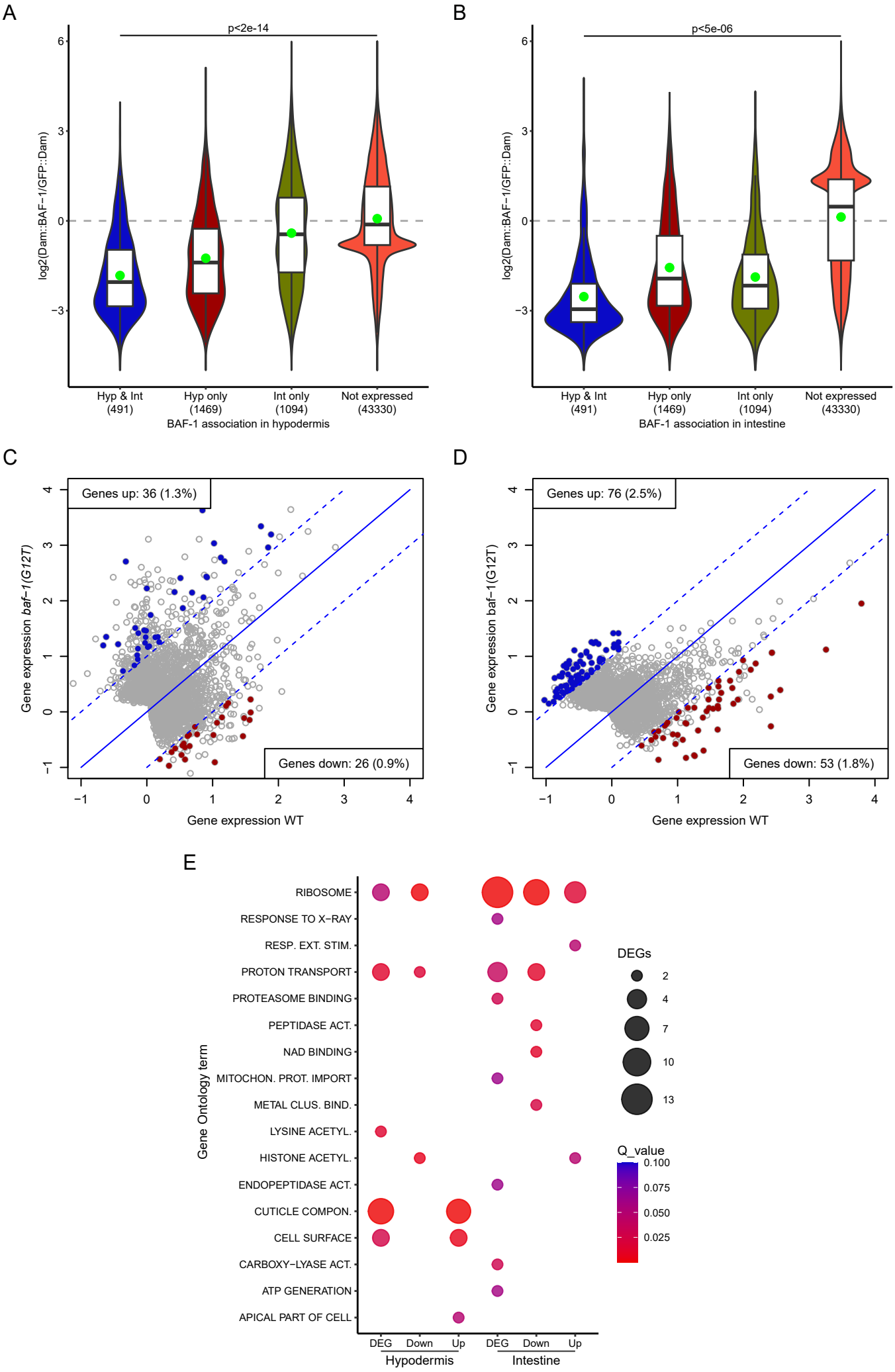
A
p<2e-14
log2(Dam::BAF−1/GFP::Dam)
Hyp & Int (491)
Hyp only (1469)
Int only (1094)
Not expressed (43330)
BAF-1 association in hypodermis
B
p<5e-06
log2(Dam::BAF−1/GFP::Dam)
Hyp & Int (491)
Hyp only (1469)
Int only (1094)
Not expressed (43330)
BAF-1 association in intestine
C
Genes up: 36 (1.3%)
Genes down: 26 (0.9%)
Gene expression baf−1(G12T)
Gene expression WT
D
Genes up: 76 (2.5%)
Genes down: 53 (1.8%)
Gene expression baf−1(G12T)
Gene expression WT
E
Gene Ontology term
RIBOSOME
RESPONSE TO X−RAY
RESP. EXT. STIM.
PROTON TRANSPORT
PROTEASOME BINDING
PEPTIDASE ACT.
NAD BINDING
MITOCHON. PROT. IMPORT
METAL CLUS. BIND.
LYSINE ACETYL.
HISTONE ACETYL.
ENDOPEPTIDASE ACT.
CUTICLE COMPON.
CELL SURFACE
CARBOXY−LYASE ACT.
ATP GENERATION
APICAL PART OF CELL
DEG Down Up DEG Down Up
Hypodermis
Intestine
DEGs
2
4
7
10
13
Q_value
0.100
0.075
0.050
0.025

Figure 6

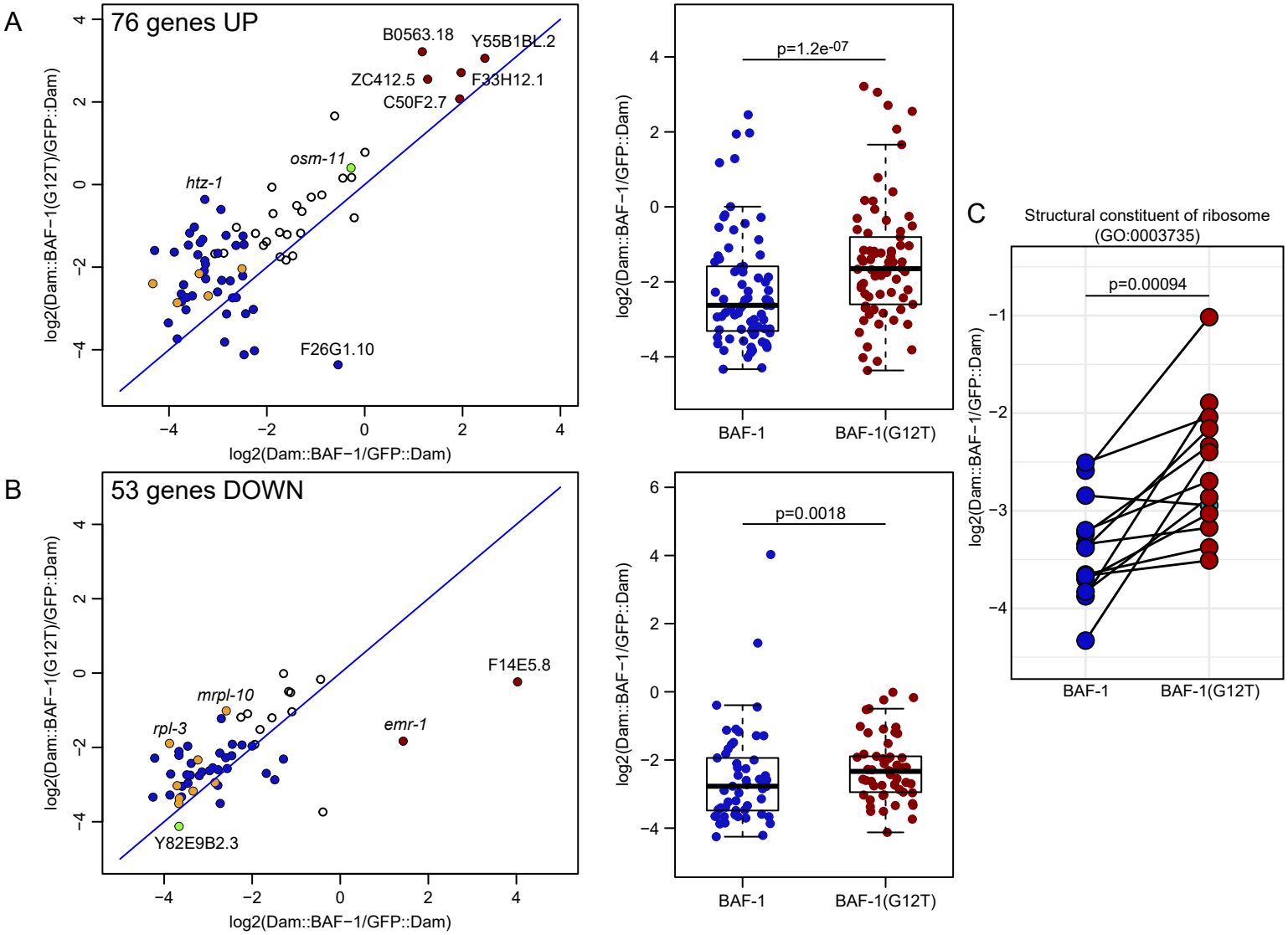
A
76 genes UP
B0563.18
Y55B1BL.2
ZC412.5
F33H12.1
C50F2.7
osm-11
htz-1
F26G1.10
log2(Dam::BAF−1(G12T)/GFP::Dam)
log2(Dam::BAF−1/GFP::Dam)
p=1.2e-07
BAF-1
BAF-1(G12T)
B
53 genes DOWN
F14E5.8
mrpl-10
rpl-3
emr-1
Y82E9B2.3
p=0.0018
C
Structural constituent of ribosome
(GO:0003735)
p=0.00094

Figure 7

A

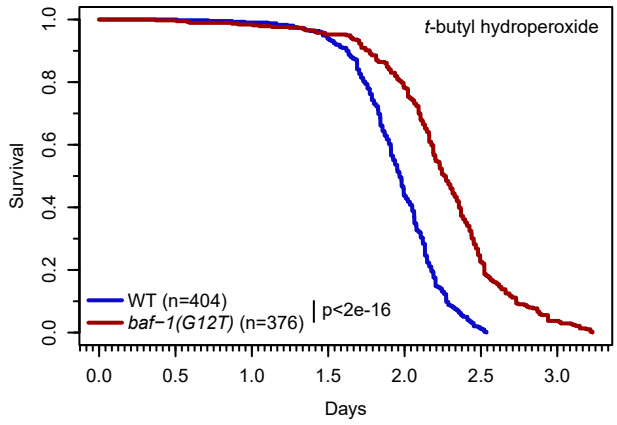
t-butyl hydroperoxide
Survival
1.0
0.8
0.6
0.4
0.2
0.0
WT (n=404)
baf−1(G12T) (n=376)
p<2e-16
0.0
0.5
1.0
1.5
2.0
2.5
3.0
Days

B

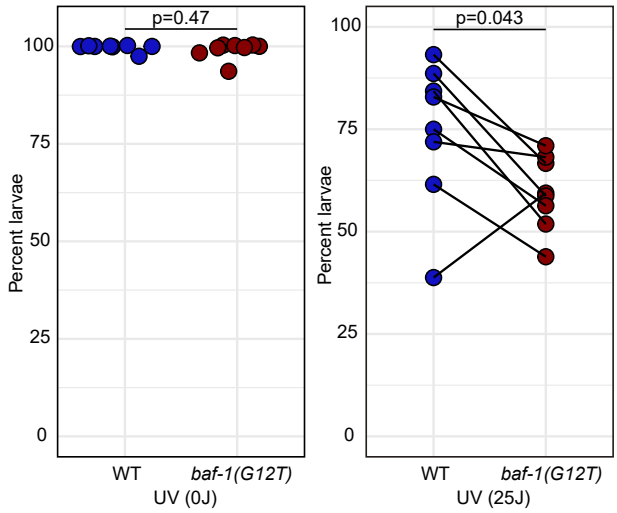
p=0.47
Percent larvae
100
75
50
25
0
WT
baf-1(G12T)
UV (0J)
p=0.043
Percent larvae
100
75
50
25
0
WT
baf-1(G12T)
UV (25J)

C

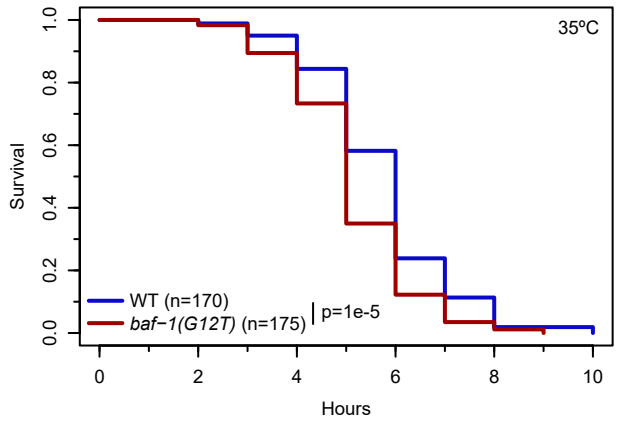
35ºC
Survival
1.0
0.8
0.6
0.4
0.2
0.0
WT (n=170)
baf−1(G12T) (n=175)
p=1e-5
0
2
4
6
8
10
Hours